Torgeir Matre Sandvik

# Development of Li$_3$YCl$_6$-Coated NCA Cathode via Mechanofusion and its Electrochemical Evaluation in Argyrodite-Based Solid-State Batteries

**NTNU**
Kunnskap for en bedre verden

Torgeir Matre Sandvik

# Development of Li$_3$YCl$_6$-Coated NCA Cathode via Mechanofusion and its Electrochemical Evaluation in Argyrodite-Based Solid-State Batteries

**NTNU**
Kunnskap for en bedre verden

# Abstract

Recent years have witnessed significant development in all-solid-state batteries (SSBs) research. However, the technical challenges including the electrode-electrolyte interface incompatibility due to (electro) chemical instabilities or lattice mismatch etc. have impeded the commercialisation of this battery technology. Benefiting from its high $Li^+$ conductivity at room temperature and ease in processibility, $Li_6PS_5Cl$ (LPSC) solid electrolyte (SE) has been a material of choice in SSB research. However, the narrow electrochemical window hinders its integration with high voltage cathodes to achieve practical energy densities. To circumvent the issues related to interface incompatibility, rare-earth halides are explored currently as promising interlayers or coating materials for high-voltage cathodes used in SSBs containing argyrodite-type SEs.

This thesis is an attempt to investigate $Li_3YCl_6$ (LYC)-coated $LiNi_{0.8}Co_{0.15}Al_{0.05}O_2$ (NCA) to facilitate LPSC in SSBs. NCA was dry-coated by mechanofusion and investigated by Focused Ion Beam-Scanning Electron Microscopy and Scanning Transmission Electron Microscopy (STEM). Pristine-and LYC-coated NCA electrodes were prepared and utilised in coin cells with state-of-the-art liquid electrolyte and in SSBs. A porous, approximately 20 nm thick and continuous coating was observed by STEM imaging of the NCA cathode coated with 3 wt% LYC. Liquid electrolyte-containing cells delivered low initial discharge capacity of $120.2 \, \mathrm{mA\,h\,g^{-1}}$ and $117.2 \, \mathrm{mA\,h\,g^{-1}}$ for cells with 1.5 wt% and 3 wt% LYC-coating, respectively. Initial Coulombic efficiency (ICE) was 31.1% and 39.4%, respectively. Initial discharge capacity of the pristine NCA cycled in liquid electrolyte-containing cells was $176.4 \, \mathrm{mA\,h\,g^{-1}}$ and ICE was 89.6%. On the other hand, SSBs showed significant improvement in discharge capacity from $8.50 \, \mathrm{mA\,h\,g^{-1}}$ for pristine NCA to $100 \, \mathrm{mA\,h\,g^{-1}}$ and $113 \, \mathrm{mA\,h\,g^{-1}}$ for 1.5 wt% and 3 wt% LYC-coated NCA, respectively, and the ICE was 8.74%, 57.8% and 56.9%, respectively. From the electrochemical investigations of the liquid electrolyte-containing cells and SSBs, it was concluded that LYC was inherently unstable in contact with NCA at the voltages utilised (4.3 V vs $Li/Li^+$) for battery cycling. Although the LYC coating significantly improved electrochemical performance of the SSBs, the gradual capacity fading indicated the possible material degradation at the electrode interface. To further improve the performance of SSBs an intrinsically stable coating material is highly desirable.

# Sammendrag

De siste årene har det vært en betydelig utvikling innen forskning på faststoffbatterier (SSB). Imidlertid har de tekniske utfordringene, inkludert inkompatibilitet i grensesnittet mellom elektrode og elektrolytt på grunn av (elektro)kjemisk ustabilitet eller gitterforskyvning osv. hindret kommersialiseringen av denne batteriteknologien. Ved å dra nytte av dens høye $Li^+$-ledningsevne ved romtemperatur og høye prosesserbarhet, har den faste elektrolytten $Li_6PS_5Cl$ (LPSC) blitt et mye benyttet materiale i SSB-forskning. Imidlertid hindrer det smale elektrokjemiske vinduet til LPSC dets integrasjon med høyspentkatoder for å oppnå praktiske energitettheter. For å omgå problemene knyttet til grensesnittinkompatibilitet, utforskes sjeldne jordartshalider for tiden som lovende mellomlag eller beleggmaterialer for høyspentkatoder brukt i SSB-er som inneholder SE-er av argyrodittype.

Denne oppgaven forsøker å undersøke $Li_3YCl_6$ (LYC)-belagt $LiNi_{0.8}Co_{0.15}Al_{0.05}O_2$ (NCA) for å fremme LPSC i SSB. NCA ble tørrbelagt ved mekanofusjon og undersøkt av Fokusert ionestråle-Scanning elektronmikroskop og Scanning transmisjonselektronmikroskop (STEM). Uberørte og LYC-belagte NCA-elektroder ble forberedt og brukt i myntceller med toppmoderne flytende elektrolytt og i SSB-er. Et porøst, ca. 20 nm tykt og kontinuerlig belegg ble observert ved STEM-avbildning av NCA-katoden belagt med 3 vektprosent LYC. Celler med flytende elektrolytt leverte lav første utladningskapasitet på 120,2 $mAh\,g^{-1}$ og 117,2 $mAh\,g^{-1}$ for celler med henholdsvis 1,5 vektprosent og 3 vektprosent LYC-belegg. Den første Coulombiske virkningsgraden (ICE) var på henholdsvis 31,1 % og 39,4 %. Den første utladningskapasiteten til cellene med uberørt NCA og som inneholdt flytende elektrolytt var 176,4 $mAh\,g^{-1}$ og ICE var 89,6 %. På den annen side viste SSB-ene betydelig forbedring i utladningskapasitet fra 8,50 $mAh\,g^{-1}$ for uberørt NCA til 100 $mAh\,g^{-1}$ og 113 $mAh\,g^{-1}$ for henholdsvis 1,5 vektprosent og 3 vektprosent LYC-belagt NCA, og ICE var henholdsvis 8,74 %, 57,8 % og 56,9 %. Fra de elektrokjemiske undersøkelsene av cellene med flytende elektrolytt og faststoffcellene, ble det konkludert med at LYC var grunnleggende ustabil i kontakt med NCA ved spenningen som ble brukt (4,3 V vs Li/Li$^+$) for batterisykling. Selv om LYC-belegget betydelig forbedret den elektrokjemiske ytelsen til SSB-ene, indikerte den gradvise kapasitetsforverringen en sannsynlig materialforringelse i grensesnittet mellom katode og LYC. For å ytterligere kunne forbedre ytelsen til SSB-er er et grunnleggende stabilt beleggmateriale svært ønskelig.

# Preface

This master's thesis is a continuation of my work during TMT4500 Materials Technology, Specialization Project. It is a mandatory task to graduate with a master's degree in Industrial Chemistry and Biotechnology at the Norwegian University of Science and Technology. The work was undertaken from January to June 2022. I would like to thank my supervisor, Associate Professor Daniel Rettenwander and co-supervisor Postdoctoral Fellow Mir Mehraj Ud Din for their help and ideas throughout the thesis. I would also like to thank the rest of the Rettenwander group, PhD Candidate Florian Flatscher, PhD Candidate Jin Feng and PhD Student Hung Quoc Nguyen for their help. The FIB work was done by Sigurd Wenner within the Norwegian Micro- and Nano-Fabrication Facility, NorFab (RCN, grant 245963/F50). The TEM work was carried out by Sigurd Wenner at the NORTEM (RCN, grant 197405) infrastructure at the TEM Gemini Centre, Trondheim, Norway.

# Contents

# Chapter 1

# Introduction

Despite the Covid-19 pandemic being at the centre of attention for the last two years, the consequences of climate change are just as relevant today as they were back in 2019 before the pandemic. Transitioning from an unsustainable, "fossil fuel"-dependent society to a sustainable, carbon neutral (or even negative) society, is a massive challenge. A large part of this transition will be in the transportation -and energy sectors.

According to research by Rystad Energy, demand for electric vehicle (EV) batteries is expected to be 4.9 TWh by 2030, a 13× increase from the 2021 level of 373 GWh. Similarly, demand for stationary battery storage is expected to increase from 139 GWh in 2021 to 2.5 TWh in 2030. Stationary storage is becoming more important as backup energy and grid-stabilising needs are growing with the use of intermittent power sources for electricity generation, such as wind and solar[13].

Although electric vehicles are the least likely to catch fire (25.1 per 100k sales versus 3474.5 for hybrid vehicles and 1529.9 for internal combustion engine vehicles)[4], with the rapidly growing EV demand, safer batteries are still highly desirable. The flammable nature of commonly used carbonate electrolytes together with polymer separators, pose a fire hazard risk for today's conventional lithium-ion batteries (LIBs)[24]. A much researched potential solution is the solid-state battery (SSB) with inorganic solid electrolytes (SEs) that are non-flammable. Some researchers have also claimed SSBs enable the use of lithium metal (Li) anodes instead of graphite, which will greatly improve gravimetric and volumetric energy density.

Among the state-of-the-art SEs, with comparable ionic conductivity to liquid elec-

trolytes, are several sulfides, e.g. $Li_6PS_5Cl$ and $Li_{10}GeP_2S_{12}$[45]. Unfortunately, these SEs are highly unstable in contact with high voltage cathode materials. A common strategy to protect these sulfides from degradation and enable their use is to apply a protective coating on the cathode particles. One of the materials that have recently attracted interest is $Li_3YCl_6$ (LYC), due to its promising combination of a high oxidation limit of 4.21 V (vs Li/Li$^+$), as well as a relatively high ionic conductivity of $0.51\,mS\,cm^{-1}$[1].

# Aim of this work

The aim of this thesis is first to utilise the nanoscale, amorphous LYC-particles, synthesised mechanochemically during the specialisation project, for dry-coating of NCA-particles by mechanofusion. The coated particles will be investigated by a wide range of characterisation techniques such as SEM, FIB-SEM, TEM and STEM with element mapping to understand the difference between pristine and coated NCA particles in terms of particle shape, coating thickness and coating uniformity. Secondly, coin cells with liquid electrolyte and solid-state cells with solid electrolyte will be fabricated utilising pristine -and LYC-coated NCA cathodes and their electrochemical performance will be compared. It is anticipated that the assembled SSBs containing LYC-coated NCA cathodes will deliver enhanced electrochemical performance in regards to ICE and longer cycle life, compared to the ones with pristine NCA cathodes. Galvanostatic cycling with potential limitation (GCPL) will be utilised to charge and discharge the batteries. Potensiostatic electrochemical impedance spectroscopy (PEIS) will be utilised to highlight the differences in internal resistance between the cells with uncoated cathode particles and coated cathode particles, before and after GCPL measurements.

# Chapter 2

# Theory

## 2.1 Li-ion batteries

### 2.1.1 General overview and operating principle

A LIB is a form of energy storage device that allows electrical energy to be transformed into and stored as chemical energy. LIBs are rechargeable batteries, meaning that they allow for recharging and discharging many times. The commercialisation of these batteries has enabled mobile communication devices, cameras and audio devices, the use of battery electric vehicles and grid stability for intermittent power sources such as wind and solar.

The battery consists mainly of two electrodes, an electrolyte, and a separator. In addition, components like electrode binders, conductive agents and current collectors are present. The electrodes are where the electrochemical reactions take place inside the battery. At the positive electrode, lithium is extracted from the material during charging, and inserted or intercalated during discharging. Simultaneously, $Li^+$ intercalate into the negative electrode during charge and deintercalate during discharge[15].

For the transport of ions, the electrolyte is essential. It has two main tasks:

- It acts as the ionic contact between the two electrodes inside the cell, resulting in a closed circuit once the battery is connected to an external load/power source.

- It acts as an electronic insulator and in some cases separator to prevent any direct electrical contact between the electrodes in the cell that otherwise could result in a short-circuiting and thermal runaway.

For liquid electrolytes, a solid, porous dielectric material is normally utilised as the short-circuit barrier between the electrodes. In addition to the main tasks of the electrolyte, some critical requirements are[12]:

- It should ideally be inert to the other cell components, especially the positive and negative electrodes and the current collectors.

- It should remain in the liquid phase over the operating temperature range of the cell.

- It should to a large extent dissolve lithium salts and have a high ionic conductivity for $Li^+$ transport.

The current collectors are metallic to efficiently transport electronic current to/from where the reactions take place and the external circuit. To aid with the electron transport between the active material and the current collectors, small amounts of conductive agents are mixed together with the active material. The current collectors and conductive agents should be chemically and electrochemically stable during operation, but the formation of a passivating layer on the current collectors is also normal. Electrode binders are also mixed with the active material and the conductive agents. They ensure a homogeneous distribution of particles during the fabrication process. They also ensure cohesion between the active material particles and adhesion between the active material and the current collectors[9]. As previously mentioned, a dielectric separator is utilised to physically separate the two electrodes to ensure no direct electronic contact between the them[15]. A schematic illustration of the first commercial LIB is shown in Figure 2.1.1.

The driving force for operation of a battery is the difference in electrochemical potential between the anode and the cathode. The open-circuit voltage of the battery is given by

$$V_{\text{oc}} = \frac{\mu_A - \mu_C}{e},$$ (2.1.1)

where $\mu_A$ and $\mu_C$ is the electrochemical potential of the anode and cathode, respectively and e is the elemental charge of an electron.

A larger open-circuit voltage will benefit the amount of stored energy in the battery, as will be evident in Equation 2.1.6, but stability considerations of the electrolyte will be important. The electrolyte is in contact with both the anode and cathode in a battery cell. For it to remain inert and act only as an ion conductor during operation, two conditions must be met. The lowest unoccupied molecular orbital (LUMO) of the
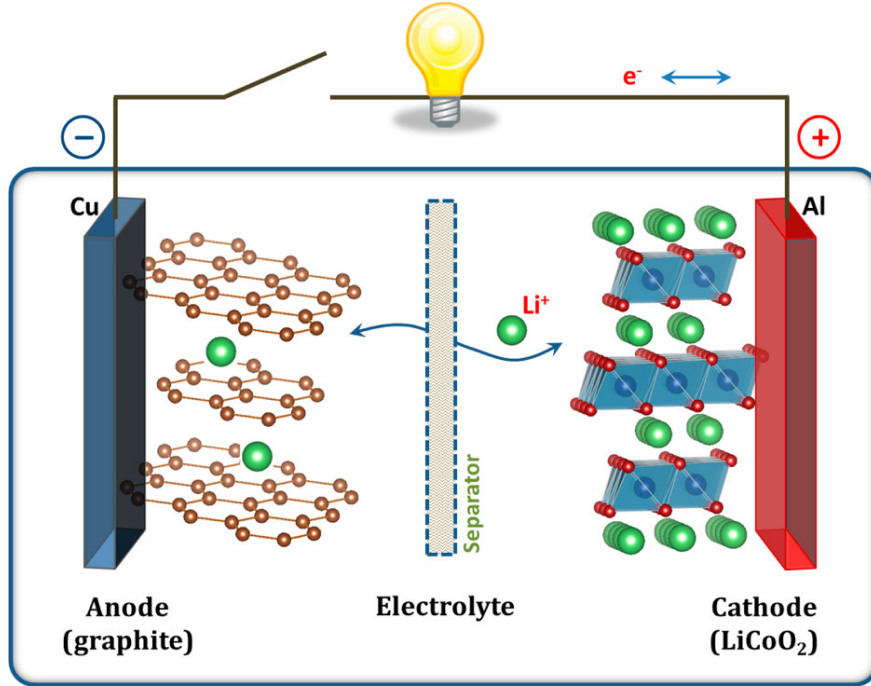
4

**Figure 2.1.1:** Schematic of a $LiCoO_2$/graphite LIB. During operation, $Li^+$ are shuffled between the layered crystal structures of the electrodes. The $LiCoO_2$ cathode is connected to an Al current collector while the graphite anode is connected to a Cu current collector. Figure from [15].

electrolyte must be at a higher energy level than $\mu_A$ and the highest occupied molecular orbital (HOMO) must be lower than $\mu_C$. If the LUMO of the electrolyte is lower than $\mu_A$ it becomes energetically favourable for electrons to "jump" from the anode to the electrolyte. This results in reduction of the electrolyte, thus forming the SEI layer in modern LIBs. If the HOMO of the electrolyte is higher than $\mu_C$, electrons from that orbital are favoured to "jump" to the cathode, creating an oxidised layer at the cathode-electrolyte interface [15]. Figure 2.1.2 illustrates this electrochemical window where LUMO and HOMO of the electrolyte determines the limits.

When a battery is charged, the charging voltage ($V_{ch}$) needed to reverse the chemical reactions inside the battery is higher than the $V_{oc}$. Similarly, the discharge voltage ($V_{dis}$) of the battery during use is lower than the $V_{oc}$. These differences are due to a polarisation $\eta$, where

$$V_{dis} = V_{oc} - \eta(q, I_{dis}) = V_{oc} - I_{dis}R_{int} \tag{2.1.2}$$

and

$$V_{ch} = V_{oc} + \eta(q, I_{ch}) = V_{oc} + I_{ch}R_{int}. \tag{2.1.3}$$

The polarisation is a function of both the state of charge of the battery q and the charge
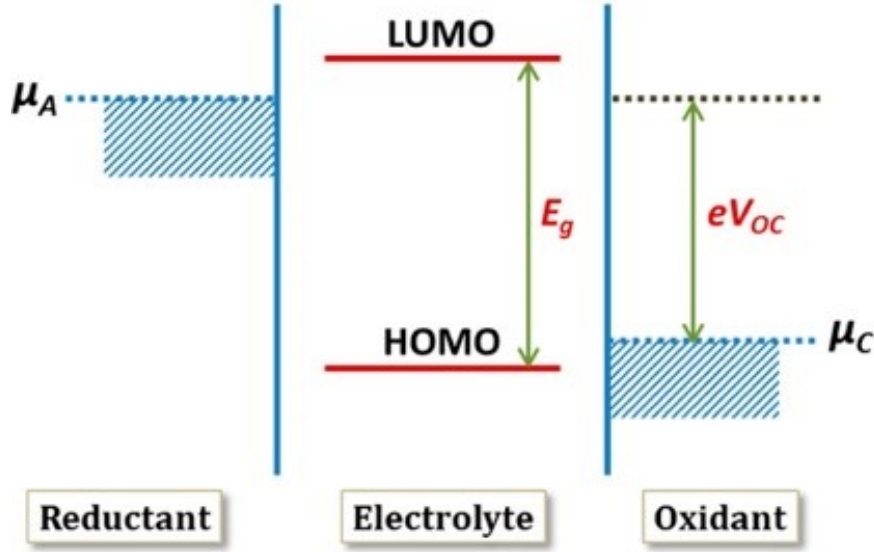
**Figure 2.1.2:** Illustration of the electrochemical stability window, $E_g$, of an electrolyte, determined by the LUMO and HOMO energy levels of the material. The stability window limits the electrochemical potential of the cathode and anode that will allow for stable operation of a battery cell. Figure from [15].

or discharge current $I_{ch}$ or $I_{dis}$, respectively. $R_{int}$ is the internal resistance of the battery. The stored or extracted amount of charge in a battery is calculated as

$$Q = \int_0^{\Delta t} I dt = \int_0^Q dq \qquad (2.1.4)$$

where Q is the total charge, often divided by unit weight ($mA\,h\,g^{-1}$) or by volume ($mA\,h\,cm^{-3}$). Reversible capacity loss occurs due to the diffusion limitations of ion transfer across the electrode-electrolyte interfaces at large currents. In addition, irreversible capacity loss takes place during cycling. Due to (electro)chemical reactions between the electrodes and the electrolyte, solid electrolyte interphase (SEI) layers form. The process consumes $Li^+$ in the cell and increases cell impedance. During cycling, the electrode particles also expand and shrink, and these volume changes cause internal stress which can result in particle cracking. The volume changes can also break apart the SEI layer, exposing fresh electrode surface to the electrolyte, forming new SEI and consuming more $Li^+$ in the cell. The Coulombic efficiency (CE) of a charge/discharge cycle is given as

$$CE = 100 \cdot \frac{Q_{dis}}{Q_{ch}} \qquad (2.1.5)$$

and can give indications of how much of the charge capacity contributed to the reversible reaction inside a battery cell, and how much went to irreversible reactions

and heat generation. A natural expansion from stored charge Q to stored energy is given by

$$E = \int_0^{\Delta t} I V(t) dt = \int_0^Q V(q) dq \qquad (2.1.6)$$

where the battery voltage is a function of the state of charge of the battery, as well as the current[15].

### 2.1.2 Cathode materials for Li-ion batteries

For LIBs, the most common cathode materials utilised are divided into three categories: layered metal oxides, olivine phosphates and spinels. The layered $LiCoO_2$ was first utilised in 1980 with a practical specific capacity of up to 160 mAh g$^{-1}$, but a continuous development of the cathode material has allowed for higher practical capacity or average voltage. Part of the Co has been replaced with Ni and Mn to create e.g. $LiNi_{0.33}Co_{0.33}Mn_{0.33}O_2$ (NCM111) or replaced with Ni and Al to create e.g. $LiNi_{0.8}Co_{0.15}Al_{0.05}O_2$, both allowing for higher practical capacities. $LiNi_{0.5}Mn_{1.5}O_4$ has a voltage plateau at 4.7 V (vs Li/Li$^+$). Lowering or eliminating the Co content in the cathode material also lowers the cost due to the high price of the raw material[8].

For the layered oxides, the general formula is $LiMO_2$, where M is Co, Ni, Mn and Al. The crystal structure, shown in Figure 2.1.3, has alternating layers of Li and transition metals in the (111) planes of the rock salt structure. The layer structure allows for reversible extraction and insertion of Li$^+$ through 2D diffusion pathways during battery operation[26].
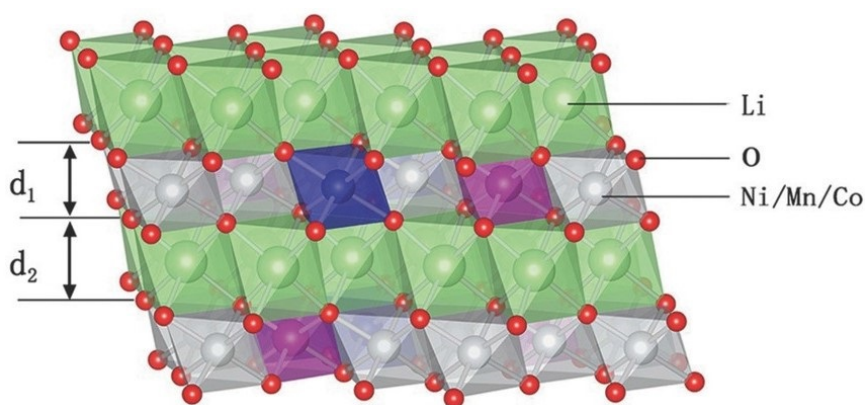


**Figure 2.1.3:** Crystal structure of layered transition metal oxides. Here a mix of Ni, Co and Mn is in the transition metal layers. Figure from[10].

As mentioned, substitution of Co and Al in the layered $LiNiO_2$ structure creates the NCA cathode material. Cobalt ensures more structural ordering by keeping more of

the $Ni^{2+}$ out of the Li layer. Due to the similar ionic radii of $Ni^{2+}$ and $Li^+$, the Ni-ions can enter the Li layer of the crystal structure, resulting in path blocking and decreased available Li for storing charge. The added aluminium is inactive in the redox reactions and helps to prevent all the Li to be removed from the crystal structure during charging. If the amount of Li in the material becomes too low, the crystal structure is destabilised and this can worsen the cyclability of the battery[26].

Within the olivine phosphate family of the $Mg_2SiO_4$-type, $LiFePO_4$ (LFP) has received a revived interest as a cathode material for LIBs in recent years. Benefits of low cost, non-toxicity and increased safety due to a higher abuse tolerance are making them suitable for electric vehicles and stationary energy storage. However, due to the bonding structure of LFP, it has low electronic and ionic conductivity which early posed an issue for the rate capabilities of the material.
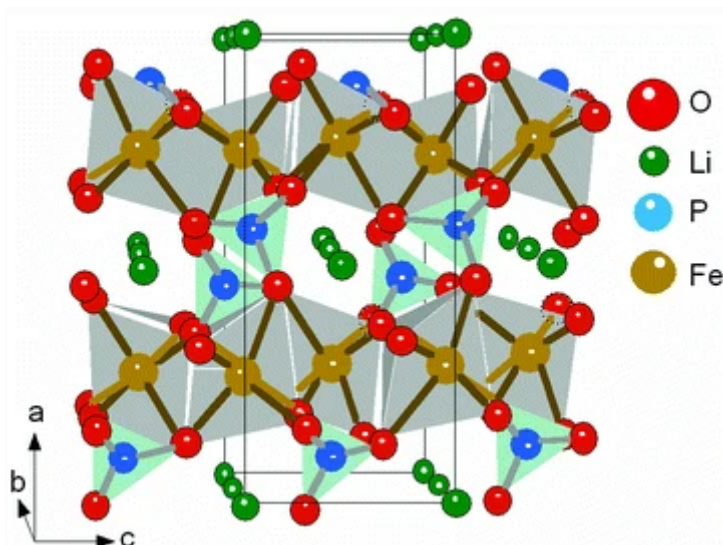


**Figure 2.1.4:** Crystal structure of $LiFePO_4$. $FeO_6$-octahedras are linked in the bc-plane by corner-sharing of O-atoms. Lithium ions are located in 1D-channels as $LiO_6$-octahedra chains. Figure from[46].

LFP has the space group *Pnma*, as shown in Figure 2.1.4. It has a distorted hcp oxygen framework with Li and Fe in half of the octahedral sites and P in 1/8 tetrahedral sites. The low electronic conductivity is due to the high ionicity of the bonding in the material, while the ionic conductivity is due to the 1D nature of the diffusion channels for $Li^+$ transport. To improve the conductivity of the material, nano-sized particles are synthesised with a thin surface coating of typically an amorphous carbon layer. The size reduction of LFP particles increase the contact area between the particle surface and the electrolyte and the small size shortens the diffusion pathway for the $Li^+$ during
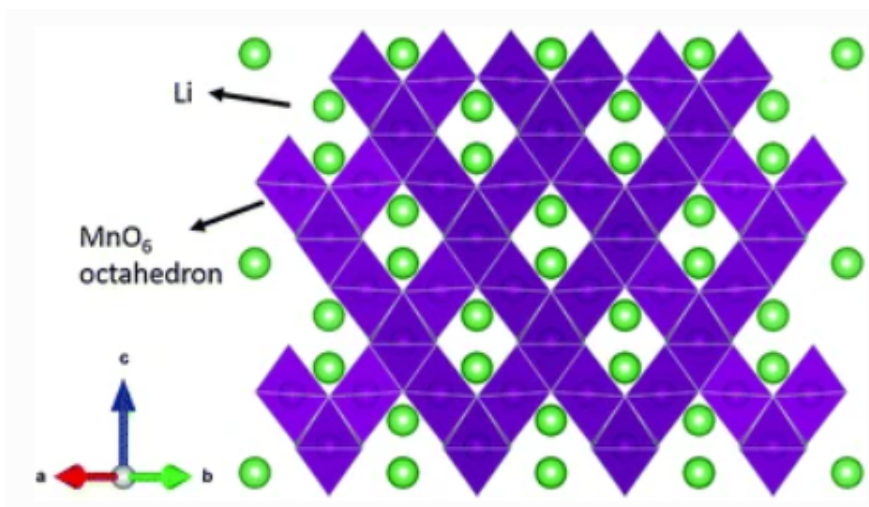
**Figure 2.1.5:** Crystal structure of spinel $LiMn_2O_4$. Mn ions are in the octahedral sites, while $Li^+$ are in tetrahedral sites, face-sharing vacant octahedral sites. Figure from[26].

operation. The coating layer helps with electronic conductivity and may decrease the "charge transfer"-resistance at the electrode-electrolyte interface[46].

Spinel $LiMn_2O_4$ was discovered as a potential cathode material by Thackray et al. in 1984. The material has the space group $Fd - 3m$, with the so called cubic spinel structure as shown in Figure 2.1.5. The structure consists of a ccp anion lattice of oxygen ions. Octahedral sites are occupied by Mn ions, however 25% of them are left vacant in the transition metal layer and 25% of them are in the Li layer. Li ions occupy the tetrahedral sites in the Li layer that are face-sharing with the vacant octahedral sites in the transition metal layer. This results in a 3D $Li^+$ diffusion network for extracting and inserting Li during operation of the battery. For pure $LiMn_2O_4$, the Mn exists as 50% $Mn^{3+}$ and $Mn^{4+}$. Introducing 25% Ni to the structure will leave all Mn as $Mn^{4+}$ and Ni as $Ni^{2+}$, creating $LiNi_{0.5}Mn_{1.5}O_4$ (LNMO). The voltage of the material can be raised to 4.7 V (vs $Li/Li^+$), thus increasing the energy density compared to $LiMn_2O_4$ with a voltage plateau of approx. 4.1 V. The capacity of LNMO is also higher than $LiMn_2O_4$[26].

## 2.1.3 Anode materials for Li-ion batteries

Due to the nature of LIBs, careful selection and engineering of the anode material is paramount to the operation of the cell. The combination of cost, availability and properties of graphite has made it the standard anode material. The large distance between graphene layers allow for the reversible insertion and extraction of $Li^+$ with relatively low volume change. However, other mechanisms and materials for Li storage are

being researched and developed.

In the early days of LIB research, theories for the good rechargeability of these batteries were that they operated with little losses, but many studies have shown otherwise. As described in Section 2.1.1, SEI formation occurs from the reaction between the electrolyte and the electrodes. The reduction of electrolyte in contact with the anode is a major source of irreversible capacity loss, but does still allow for $Li^+$ to pass through. The SEI also protects the electrode from solvent molecules, which otherwise could exfoliate the graphite if allowed to intercalate. If made correctly, the cell is passivated by the SEI and it allows for stable cycling as long as the layer remains intact[30].

The graphite structure consists of graphene layers weakly connected by van der Waals forces. The carbon atoms in the graphene layer are $sp^2$ hybridised. The unlocalised $\pi$-electrons in the graphene layer gives rise to the unusually high electronic conductivity. The carbon atoms are connected in hexagon rings. When fully charged, six carbon atoms hold one Li. The theoretical specific capacity of graphite then becomes approximately $372\,\text{mA}\,\text{h}\,\text{g}^{-1}$.

The Li insertion/extraction process is given by Equation 2.1.7

$$Li^+ + e^- + nC = LiC_n, \tag{2.1.7}$$

where n is between 6-12 depending on the stage of the insertion/extraction process. In the beginning of the intercalation process, Li is inserted into different graphene layers, but as more and more Li is inserted, every layer fills up. The different types of carbon structures possess varying amounts of graphene layers in the stack and with varying continuous graphene layers, resulting in different Li storage capacities and rate performances.

Alloy anodes have two to ten times higher specific capacity compared to carbon anodes. The reason for the potentially very high specific capacity of these anodes comes from the way Li is stored. It is by the reaction

$$nLi^+ + ne^- + M = Li_nM, \tag{2.1.8}$$

where n can be a number greater than 1 and M is the alloying material. Some of the anode materials are Al, Sn, Mg and In. The higher redox potential of these alloys helps to prevent direct Li plating and dendrite formation, increasing the safety of the

batteries. However, these types of anodes do not come without their own issues. Their low electronic conductivity and large volume expansion/contraction during charging and discharging can lead to high internal resistance and rapid capacity loss.

Conversion-type anode materials (CTAMs) such as transition metal sulphides, oxides, phosphides, nitrides, fluorides and selenides have been given increasing interest in recent years. As many of the CTAMs exist naturally they are relatively cheap to produce. Also, these anode materials do not experience Li dendrite formation during operation like alloy anodes, resulting in safer LIBs. They do however also have some challenges. A major drawback of CTAMs is their large voltage hysteresis. It ranges from hundreds of mV to 2V, resulting in very low efficiency of charging and discharging the battery. Intercalation anodes like graphite usually have voltage hysteresis of a few tens of mV, for comparison[30].

Li metal is theoretically one of the most ideal anode materials, with a redox potential of $-3.04\,\mathrm{V}$ (vs SHE) as well as a specific capacity of $3862\,\mathrm{mAh\,g^{-1}}$. The anode reaction is simply

$$x\mathrm{Li} = x\mathrm{Li}^+ + x\mathrm{e}^-, \tag{2.1.9}$$

however, the plating process of Li may form dendrites. During discharge not all dendrites formed may be "stripped" and can become so called dead Li, unable to act as charge storage anymore. Over time, the dendrites can grow long enough to penetrate the separator and cause a short-circuit of the cell. Li metal is also very reactive, due to its extremely low redox potential. It will react with any electrolyte and create an SEI layer made of reduction products of the electrolyte. Because of the large volume expansion of the anode during operation, the SEI layer experiences huge stresses and will crack. This opens the SEI for new electrolyte to be reduced in contact with the Li anode. The result is more consumption of $\mathrm{Li}^+$ in the electrolyte, as well as increased internal resistance due to the excessive amount of SEI over time. Uneven SEI formation leads to inhomogeneous conductivity and current density while plating Li during charging. The dendrite growth process and how it might cause an internal short-circuit is illustrated in Figure 2.1.6[43].

### 2.1.4   Electrolytes for Li-ion batteries

With the very negative potentials of lithiated anode materials, aqaueous electrolytes are not utilised in LIBs. Usually, several aprotic organic solvents are utilised together with some dissolvable Li salt. However, since the charging potential of graphite is very
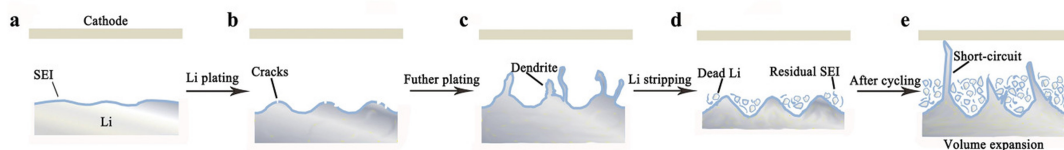
**Figure 2.1.6:** Illustration of the course of events causing a short-circuit in a cell using a Li metal anode. a) Initial SEI layer formation. b) Cracks are formed due to volume expansion of the anode during Li plating. c) Dendrites form from increased plating at crack points. d) Dead Li and SEI is left after stripping. e) An eventual short-circuit occurs as dendrites grow long enough to contact the cathode. Figure from [43].

negative, even though it is higher than (Li/Li$^+$), most of the electrolytes utilised are still reduced in contact with the electrode. The SEI layer is still forming to passivate the cell from further decomposition reactions. Since the passivation role of the SEI layer is critical for a long cycle life in LIBs, the electrolyte's ability to form a stable and highly ionically conductive SEI layer is a major factor to determine the usefulness of the electrolyte in a battery cell.

The cyclic ethylene carbonate (EC) is a very common solvent due to important properties such as large dipole moment, good salt solubility, low vapour pressure and most importantly the ability to form a good SEI layer at the interface with graphite. However, the solvent comes with some drawbacks, including a high melting point and viscosity, thus limiting cold weather performance by itself. Therefore, it is normally combined together with linear carbonates like dimethyl carbonate (DMC), ethyl methyl carbonate (EMC) or diethyl carbonate (DEC), which improve liquid phase range of the electrolyte and ionic conductivity [18]. The most common cyclic and linear molecules utilised as solvents are shown in Figure 2.1.7.
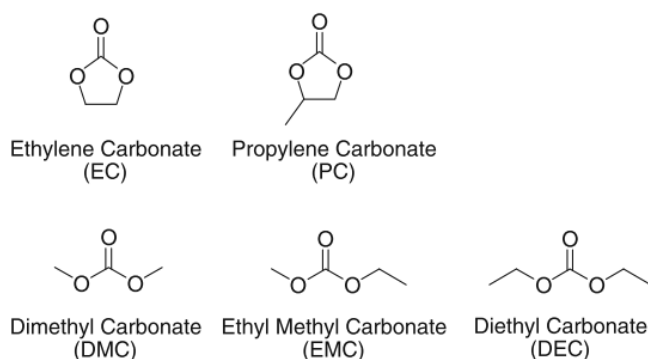


**Figure 2.1.7:** Most common cyclic and linear electrolyte solvents utilised for LIBs. Figure from [18]

The Li salt in the electrolyte dissociates into a Li cation and a very anodically stable

anion. This is because they are usually a Li conjugate base of a super acid. Lithium hexafluorophosphate (LiPF$_6$) is the mainly utilised salt for LIBs. It has a high solubility in the solvents shown in Figure 2.1.7, good ion mobility and is not easily reduced or oxidised at the electrodes. The PF$_6^-$-anion also reacts with the aluminium current collector to form a passivating AlF$_3$ layer that prevents corrosion in the alkaline environment.

### 2.1.5   Thermal hazards of Li-ion batteries

LIBs are generally operated safely, with hundreds and thousands of charge/discharge cycles without any issues. However, some critical factors can affect the normal operation of these batteries, ultimately resulting in thermal hazards. They are physical, electrical and thermal factors, as well as manufacturing defects and battery ageing.

A physical factor can be an applied force on the battery due to e.g., an electric vehicle collision that deforms one or several batteries or makes a sharp object surrounding the battery penetrate the outer casing. The deformation can result in the electrodes coming in direct contact to cause a short-circuit or the flammable electrolyte may leak through the broken cell casing to induce a fire. Penetration of a battery cell has often resulted in a more severe short-circuit with accompanying severe fire.

Electrical factors can be e.g., external short-circuit, overcharging the battery or discharging it too low. An external short-circuit may be caused by battery deformation, water intrusion or simply improper usage and wiring. The battery will discharge at a current that is much higher than normal operation and the internal battery impedance will generate a substantial amount of heat. A rapid temperature increase will cause the electrolyte and electrodes to react exothermally to further increase the temperature. With a malfunctioning or poorly made battery management system (BMS), batteries can be charged to above the upper cut-off voltage set for safe operation. Continued charging leads to internal pressure build-up, accelerated battery degradation and lower performance. The significant Li extraction from the cathode leads to structural collapse and release of oxygen gas. The thermal hazard with a fully charged battery is a much more severe situation than a discharged battery due to all the stored energy. Similarly, over-discharge may be due to the BMS system and will extract too much Li, this time from the anode. Gases such as CO and CO$_2$ can form and cause pressure build-up and battery swelling.

A high external temperature and overheating of the battery due to improper cooling system of the battery or unsafe operating conditions may lead to thermal failure. Even-

tually, the battery components will decompose, and side reactions will release more heat to finally cause a thermal runaway inside the battery.

Conventional LIB components like plastic parts, electrolyte and separator are combustible and therefore pose fire hazards. Previous studies have reported that the initial decomposition temperature of organic solvents was approximately 80 °C and that they could further react exothermally with the electrodes to cause a thermal runaway, where the heat released from the exothermic reaction facilitates further reactions and continuous temperature increase[31].

Since the organic carbonates like DMC, EMC, DEC, EC and PC are highly flammable, a logical countermeasure has been to add fire retardant (FR) components. Unfortunately, the same requirements that apply for the other electrolyte components for the performance of LIBs also apply to the FR component. Finding FRs with high electrochemical stability, high ionic conductivity, low cost etc. is equally challenging[31].

## 2.2   All-solid-state batteries

### 2.2.1   General overview, advantages and challenges

SSBs are in many ways similar to LIBs. It has a positive and negative electrode connected by an electrolyte, with conducting carbon for improved electronic conductivity from the cathode/anode particles to the current collectors. Figure 2.2.1 shows a simple schematic of an SSB. Cathode materials utilised are similar to LIBs to achieve high voltage batteries, with layered oxides, spinels or olivines as described in Section 2.1.2.
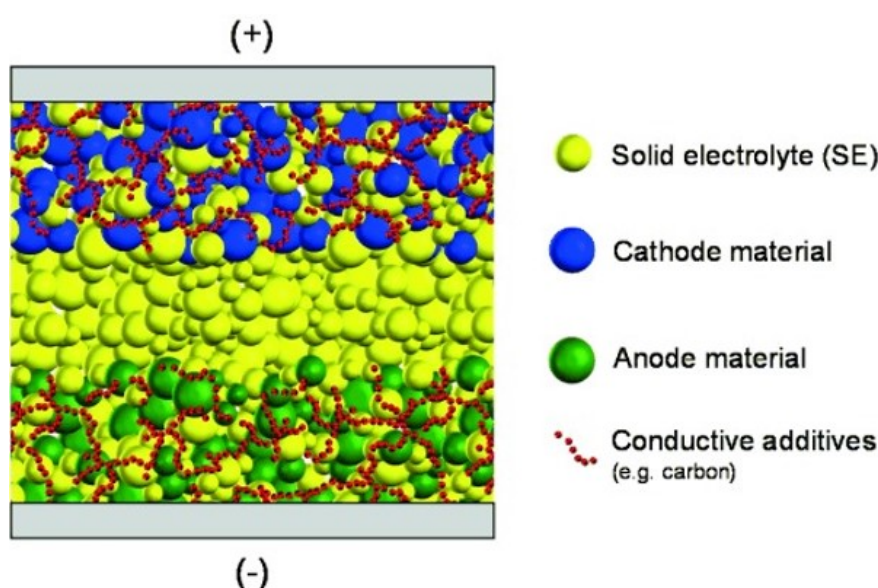


**Figure 2.2.1:** Schematic of a solid state battery. Figure from [20].

The major difference between the two technologies originates from the SE. By switching from an organic, flammable liquid electrolyte to an inorganic, non-flammable SE, an inherent safety risk that could cause battery fires is mitigated. The other difference, with regards to energy density, is the promise by SEs to inhibit Li dendrite growth to enable the Li metal as anode material. This would allow going from a theoretical capacity of approximately $372 \, \mathrm{mA \, h \, g^{-1}}$ for graphite in LIBs to $3860 \, \mathrm{mA \, h \, g^{-1}}$ for Li in SSBs [17].

To date, the issue of Li dendrite growth is still very relevant. Monroe and Newman [28] hypothesised that dendrite growth would be suppressed if the shear modulus of the SE was twice as high or more than Li metal. However, experimental results have shown dendrite growth in SEs with more than 10 times higher shear modulus than Li due to inhomogeneous dissolution and deposition of Li during cycling [14].

15

Moreover, SEs were thought to have superior electrochemical stability compared to organic liquid electrolytes, but first-principles calculations have painted a different picture. Zhu et al.[53] found that most SE-electrode interfaces were not thermodynamically stable both before and during electrochemical cycling. Calculations made between SEs and LCO showed that sulfides especially, but also some oxides were thermodynamically favoured to oxidise and that sluggish reaction kinetics was the only factor limiting reactions at the interface.

To improve long term cycling of SSBs, Li alloys are utilised to substitute the Li metal anode. Compared to Li plating, the alloy formation for Li with metals like Al, Ga, In, Sn or Sb happens at approximately 1 V or lower vs Li/Li$^+$. This lower thermodynamic driving force for SE reduction makes these alloys attractive for more stable cycling of SSBs. The risk of dendrite formation is also reduced, since the Li is consumed to form an alloy instead of plating on the surface. In recent publications, the Li-In alloy has been utilised frequently due to its high ductility and constant redox potential at $0.622\,$V vs Li/Li$^+$ over a large stoichiometric ratio between Li and In. However, due to the rarity and resulting cost of indium, commercial use of Li-In alloys is not feasible. Remaining in the two phase region of (In)-InLi was shown to be critical for stable cycling[37]. Luo et al.[25] investigated the difference between Li dendrites and Li-In dendrites. They found that Li dendrites grew vertically, relatively straight from the anode/SE interface towards the cathode side. Li-In dendrites grew laterally with denser and more uniform formation. Li dendrites were thought to form due to nonuniform Li deposition and give preferential whisker formation. Li-In dendrites formed due to volume expansion and minor interface reactions to fill grain boundaries in the SE. The difference in cycling stability for the SSB cells were staggering. The SSB with LNO coated NMC622 cathode, LPSC SE and Li anode failed after 17 cycles, while the similar cell utilising Li-In anode failed after 897 cycles[25].

### 2.2.2 Solid electrolytes

With the critical role the SE has in facilitating next generation SSBs, a review of the most researched and developed electrolyte types are discussed in this section.

Oxide-based SEs are most notably NASICON-type, Perovskite-type, Garnet-type, amorphous/glass-type and $\gamma - Li_3PO_4$-type. Common for oxide-based SEs are the low ionic conductivity relative to state-of-the-art liquid electrolyte or some of the sulfide electrolytes. They are stable in ambient atmosphere, allowing for safer SSBs compared to LIBs. The sintering process of the electrolytes needed for densification

and better contact with the electrode is energy intensive and causes detrimental side reactions that result in large interface resistance. Grain-boundary resistance is also high[45].

The NASICON structure $LiM_2(PO_4)_3$, shown in Figure 2.2.2, allows for 3D diffusion channels of $Li^+$ due to octahedral and tetrahedral site vacancies. Channel sizes in the order of the $Li^+$ radius is necessary for maximising the ionic conductivity and has been achieved by doping with trivalent ions like $Al^{3+}$, $Fe^{3+}$, $Co^{3+}$ and $Ge^{3+}$.
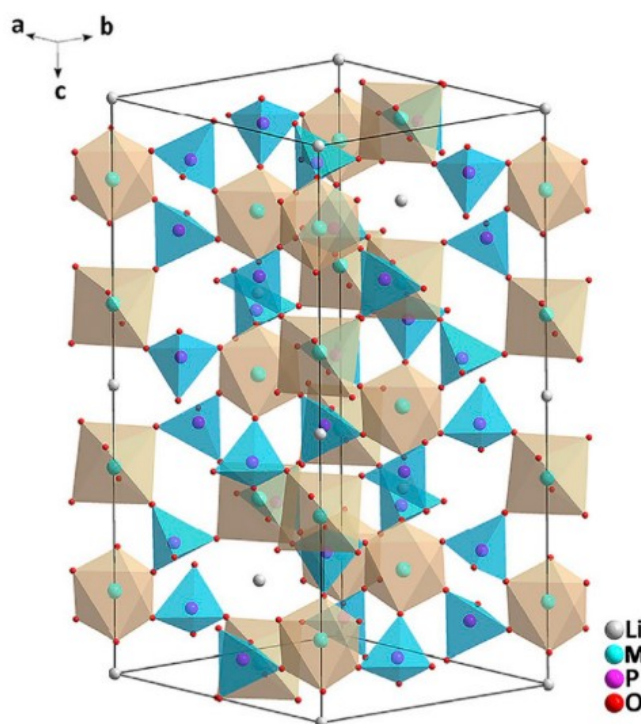


**Figure 2.2.2:** NASICON-type structure with the $LiM_2(PO_4)_3$ framework. Figure from[45].

The perovskite-type SE unsurprisingly has the perovskite crystal structure $ABO_3$, shown in Figure 2.2.3. The transition metal oxide B is centered in the $BO_6$ octahedra while the Li occupies part of the A-sites in the center of the unit cell. The perovskite structure allows for partial replacement of the A and B cations, resulting in tuned physical properties to improve ionic conductivity[45].

Sulfide-based SEs are typically divided into the materials of the $Li_2S - SiS_2$ and $Li_2S-P_2S_5$ electrolytes and the thio-LISICON family of the form $Li_{4-x}A_{1-y}B_yS_4$ with A being Si and Ge and B being P, Al, Zn and Ga. A high polarisability of the sulfide ions in these materials may create weak interaction between the anion and the $Li^+$ cation, allowing for easier transport between sites with resulting high ionic conductivities. Additionally, grain-boundary resistance is much lower for sulfide electrolytes
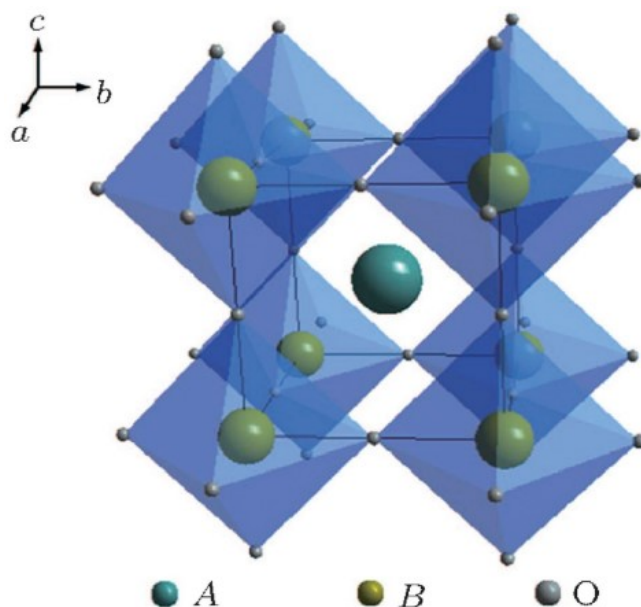
**Figure 2.2.3:** Perovskite crystal structure of the form $ABO_3$. Figure from[45].

compared to oxides. Fabrication of electrolyte pellets for use in SSBs can be made simply by cold-pressing the sulfide powder[45]. However, the intrinsic electrochemical stability window of the sulfides is very narrow. Several cyclic voltammetry reports claimed electrochemical stability above 4 V (vs Li/Li$^+$), but newer, more elaborate experiments and computational studies showed oxidation limits of less than 2.5 V (vs Li/Li$^+$)[5].

The $Li_2S-P_2S_5$ sulfide glasses were generally produced by melt quenching in vacuum sealed quartz tubes, but fabricating by mechanical milling was found to improve ionic conductivity of $75\,Li_2S-25\,P_2S_5$. This was due to the amorphous structure of the electrolyte, but the conductivity was further increased by heat treatment to form a meta-stable crystalline phase. $Li_7P_3S_{11}$, obtained by melt quenching and hot-pressing exhibited an ionic conductivity of $17\,mS\,cm^{-1}$[45]. Using stoichiometric amounts of LiCl, $Li_2S$ and $P_2S_5$ mixed by ball-milling and annealed at 550 °C, argyrodite $Li_6PS_5Cl$ was made by Koç et al.[23] with ionic conductivity of 4 $mS\,cm^{-1}$. LPSC has a cubic structure with the space group *F-43m*, but Schlenker et al.[40] also found a distortion of the $[PS_4]^{3-}$ tetrahedra by pair distribution function (DFT), resulting in a local monoclinic structure, as shown in Figure 2.2.4. Unfortunately, this family of electrolytes have very low electrochemical and chemical stabilities and reacts easily with $H_2O$ to produce the toxic gas $H_2S$.
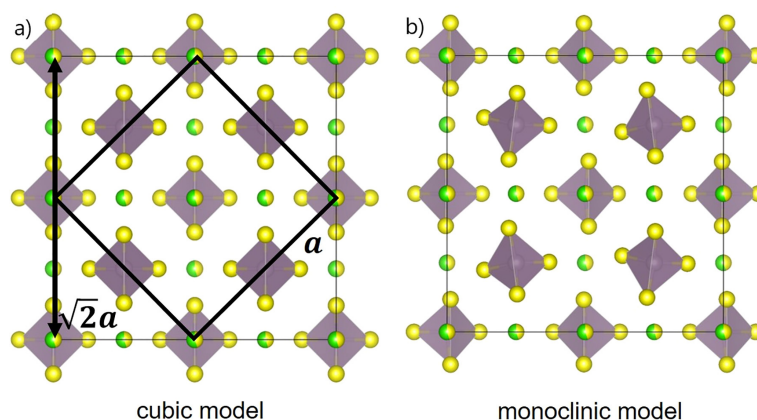
**Figure 2.2.4:** Crystal structure of LPSC (Li hidden) with (a) cubic model and (b) monoclinic model due to distortions of $[PS_4]^{3-}$ tetrahedra. $Cl^-$ are shown in green, $[PS_4]^{3-}$ tetrahedra in gray and $S^{2-}$ in yellow. Figure from 2.2.4.

As mentioned, the thio-LISICON family is based on the general formula $Li_{4-x}A_{1-y}B_yS_4$ with A = Si, Ge and B = P, Al, Zn, Ga. $Li_{3.25}Ge_{0.25}P_{0.75}S_4$ with ionic conductivity of $2.2\,mS\,cm^{-1}$, was attributed the high conductivity on vacant sites in the Li sublattice compared to the parent material $Li_4GeS_4$ [41]. A similar thio-LISICON utilising Ge, $Li_{10}GeP_2S_{12}$ (LGPS), showed an ionic conductivity of $12\,mS\,cm^{-1}$ at room temperature. However, due to the very low resource abundance of germanium, the cost of using such an element for practical solid-state batteries would be prohibitively high [45].

Solid polymer electrolytes (SPEs) consist of a solid polymer host together with Li salts. Compared to their inorganic counterparts, the SPEs typically offer better processability, higher flexibility, safety and (electro)chemical stability. Studies have also shown that SPEs can prevent Li dendrite growth, which as previously discussed is a major issue for practical SSBs. For this reason especially, SPEs have been extensively researched and improved upon. Poly ethylene oxide (PEO) and PEO-like electrolytes with Li salt are very common, but also single-ion conducting SPEs are being developed [45].

Since the first report of PEO with Li halide salts was published by Wright et al. in 1973, many different Li salts has been utilised together with the electrolyte. Studies show that the salts dissolve into their cation and anion parts and can be transported through the solvent. The ionic conductivity is however several orders of magnitude lower than oxides and sulfides, in the order of $10^{-7}\,S\,cm^{-1}$, due to crystalline regions in the polymers. Different strategies have been investigated over the years to improve the conductivity. One strategy is blending with inorganic superionic filler materials.

Another is to cause branching or cross-linking to get the PEO-like electrolytes. Blending has been an effective way to reduce the crystallinity, with increased stability and conductivity as a result[45].

Single $Li^+$ conducting-based SPEs (SLIC-SPEs) benefit from having an immobile anion framework covalently bonded to the polymer. For SPEs like PEO and the PEO-like electrolytes, both the anion and $Li^+$ cation migrates through the electrolyte and this causes concentration polarisation, affecting performance. Cao et al.[6] synthesised a SLIC-SPE with an ionic conductivity of $2.67\,mS\,cm^{-1}$ at 25 °C and oxidation limit of $5.3\,V$ (vs $Li/Li^+$)[45].

Li ternary halides have received interest as favourable SEs lately, due to their combination of high ionic conductivity as well as high (electro)chemical stability against transition metal oxide cathodes. Recent studies have reported approximately $1\,mS\,cm^{-1}$ ionic conductivity for $Li_3YCl_6$ and $Li_3YBr_6$ with wide electrochemical stability windows. The $Li_3MCl_6$ (M = In, Sc, Er and Y) showed high oxidation potentials of approximately $4.3\,V$. A graphical illustration of the electrochemical stability window of the Li halides is shown in Figure 2.2.5. Some of the promising sulfide materials are also included to illustrate the stark difference in stability. The operating potential of transition metal oxides is included for reference ( 2.5 - $4.3\,V$ vs $Li/Li^+$)[21].

### 2.2.3 Artificial cathode coating to enable high voltage SSBs

To enable the combination of superionic sulfide-based SEs and high voltage cathodes, coating layers on the surface of cathode particles have been utilised as a barrier to protect less stable bulk electrolyte materials. Acidic oxides like $Li_4Ti_5O_{12}$, $LiNb_{1-x}Ta_xO_3$ and $Li_{3-x}B_{1-x}C_xO_3$ are now commonly utilised to protect SEs from oxidation reactions at the interface between electrolyte and cathode[52]. Figure 2.2.6 illustrates how a coating layer effectively extends the stability window of the SE. If the Li chemical potential, $\mu_{Li}$ at the cathode is lower than the oxidation potential of the SE it would be favourable to oxidise the SE. An artificial coating layer between the SE and electrode could with an unfavourable oxidation of the coating material mitigate this challenge. The new electrode-electrolyte interface is between the coating material and the electrode and will only facilitate lithiation and delithiation of the electrode, as that will be the favourable reaction. The electrolyte and coating layer can be seen as a
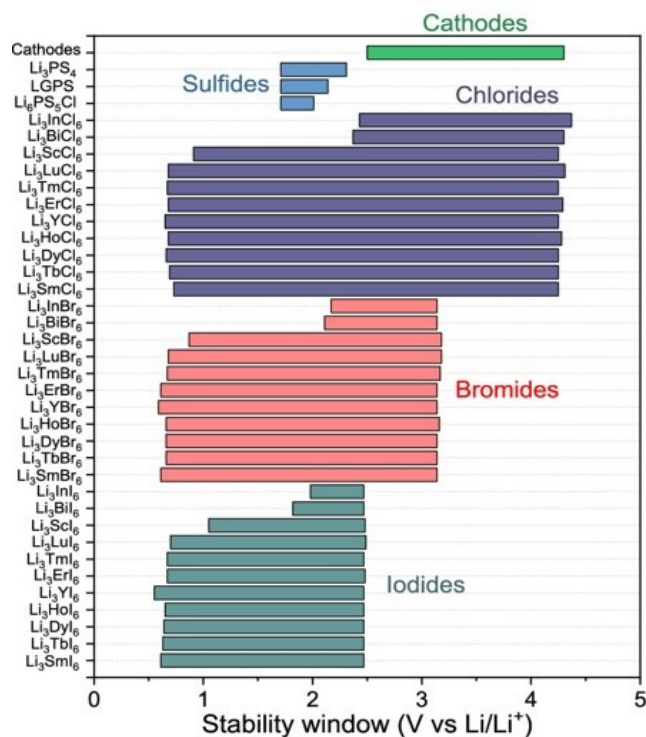
**Figure 2.2.5:** Electrochemical stability window of lithium ternary halides. Some sulfides were included for comparison. The operating potential of high voltage layered cathodes were included to illustrate the required stability window for contact with that electrode. Figure from [21].

new multilayer electrolyte with an effectively extended electrochemical stability window. If oxidation of the coating material is still thermodynamically favourable, slow reaction kinetics of the oxidation reaction can still minimise the decomposition due to the necessary overpotential required to promote the reaction, as seen in Figure 2.2.6. However, over a longer time period, the material will still deteriorate and affect the battery performance [52].

Due to the high oxidation limit of LYC of 4.21 V (vs Li/Li$^+$) [44] and relatively high ionic conductivity of $0.51\,\mathrm{mS\,cm^{-1}}$, it is a promising coating material [1]. LYC has been reported to be chemically stable in contact with LMO and LCO [21]. Asano et al. [1] fabricated LCO|LYC|Li-In SSBs that retained a capacity of 98% after 100 cycles, demonstrating the stability of LYC in contact with LCO, resulting in cycling with high Coulombic efficiency.

To apply the material, most coating techniques are wet processes that produce a waste liquid, requiring additional handling and drying. This makes the process more environmentally challenging, as well as more energy intensive. Other coating techniques
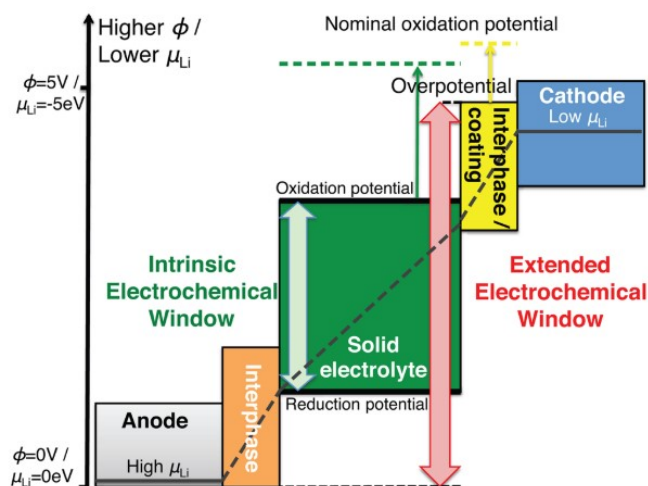
**Figure 2.2.6:** Schematic of how interphase/coating layers extend the electrochemical stability window of a SE. The lithium potentials of the cathode and anode are beyond the stability window of the SE, but not the coating layers. The observed stability window can be larger than the intrinsic due to slow reaction kinetics, marked by the green dotted line and yellow dotted line. Figure from [53].

that are commonly utilised are deposition methods, such as atomic layer deposition. Although these often provide a high degree of control during the coating process, they are costly and difficult to scale up for industrial use [50].

An effective dry particle coating technique that utilises mechanical forces for coating is called mechanofusion. It is an energy-efficient process that does not produce any waste material, due to the lack of solvent needed. Two or more powders are simply added to the device chamber. One powder acts as the "host" material, with several times larger particles than the other "guest" particles, typically micron-sized and nano-sized, respectively [50]. Inside the chamber, different types of agitators can be utilised, but the mechanism is the same. The two powders are pressed between the chamber wall and the agitator blades/hammer. At this very narrow gap between the wall and the agitator, the "guest" particles are deformed and fuses to the much larger "host" particles, due to high shear and compressive forces. Depending on the desired coating, the rotation speed and processing time can be varied and controlled. The coating process starts with a discrete coating that eventually becomes continuous as more of the "guest" particles fuse to the larger "host" particles and are deformed further. The nano-sized "guest" particles are attached firmly to the "host" particles by van der Waals interactions [33].

The minimum coating thickness is limited by the particle size of the "guest" particles. Nano-sized particles are therefore desired to achieve a thin coating, to minimise the

potential drop through the coating given by

$$V_{\text{coat}} = I \cdot R_{\text{coat}} \tag{2.2.1}$$

$$= I \cdot \frac{l}{\sigma_{\text{coat}}A} \tag{2.2.2}$$

where l is the thickness of the coating layer, $\sigma_{\text{coat}}$ is the ionic conductivity of the coating material and A is the area the current flows through. By minimising the coating thickness, the majority of the ion transport will be in the bulk electrolyte.

To achieve nano-sized LYC particles, mechanochemical synthesis by dry ball-milling can be utilised. A mechanochemical reaction is defined by a reaction taking place by absorption of mechanical energy. During ball-milling, reactant particles are broken into smaller particle sizes and simultaneously react to produce the desired product. The collisions between the reactant powder and grinding media, e.g. $ZrO_2$ balls, create tiny heat zones with enough energy to promote reactions[34].

An additional benefit of ball-milling is the generation of amorphous, meta-stable phases of the product material[38]. The material also has a high concentration of defects and structural disorders. Several researchers have found this to be beneficial for the ionic conductivity of LYC. The conductivity improvement of the amorphous LYC was mainly attributed to larger structural bottlenecks for $Li^+$ migration and a more 3-dimensional migration network, due to yttrium site disorder in the crystal structure[1][38][39].

## 2.3    Tools for battery evaluation

### 2.3.1    Galvanostatic Cycling with Potential Limitation

GCPL is the most common way of studying battery performance during charging and discharging. One of the limitations is usually a predetermined charge and discharge rate, often referred to as C-rate. A C-rate of 1 means that the battery is ideally fully charged/discharged in 1 hour. 2C is twice as fast, meaning the battery is completely charged/discharged in 1/2 hour, while 0.1C means it takes 10 hours. The potential limitations are usually set as an upper potential limit for charging and lower potential limit for discharging. For two-electrode cells, the measured voltage of the battery during cycling is what determines the upper and lower cut-off voltage[3]. After reaching the upper potential limit, the cell is often kept at this potential for some time to allow the internal cell voltage to reach the applied one[48]. The measured voltage is higher than the true cell voltage due to polarisation, as shown in Equation 2.1.3.

### 2.3.2    Electrochemical Impedance Spectroscopy

Impedance is the obstruction to current flowing in a system and consists of frequency dependent and independent contributions. For a battery system, these contributions lead to overpotentials during charge and discharge and they can be chemical and/or electrochemical in origin. They include frequency-independent resistance and frequency dependent capacitance and inductance.

Studies show a direct correlation between the internal impedance of a battery cell and it's performance in regards to rate capabilities, practical capacities and operating voltage. The way to measure the impedance of a battery is by EIS, where either an alternating current (galvanostatic EIS) or voltage (PEIS) is applied to the battery[27]. A predetermined amplitude and frequency for the alternating current or voltage is utilised and the corresponding amplitude and phase shift of the output voltage or current is observed, respectively. For PEIS, the impedance is the ratio of the sinusoidal voltage and current, given by

$$Z(t) = \frac{|\Delta E| sin(\omega t)}{|\Delta I| sin(\omega t + \Delta t)},$$
(2.3.1)

where $|\Delta E|$ and $|\Delta I|$ is the peak voltage and current amplitudes, respectively. $\omega$ is angular frequency and t is time, with $\Delta t$ representing the phase shift of the current response. A small amplitude perturbation is important for maintaining the electrochem-

ical system and minimise irreversible changes. This makes it so that an assumption of a linear relationship between voltage and current holds true[42].

For battery systems, the typical frequency range is mHz to kHz scale. In a so called Nyquist plot where the imaginary part is plotted versus the real part of the impedance, the high-frequency data is plotted first followed by repeated measurements with decreasing frequency of the applied current or voltage bias. When inductance is sub-
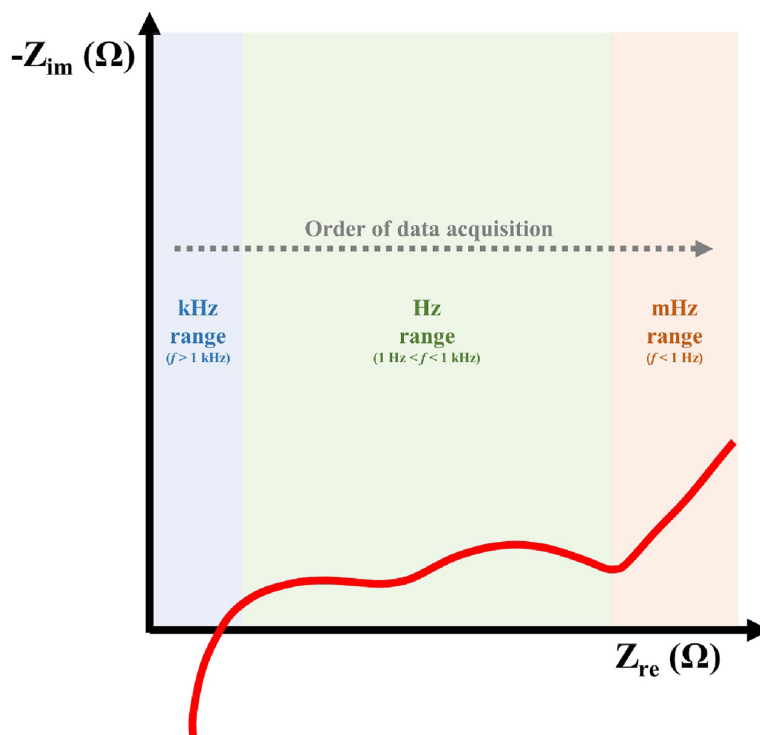


**Figure 2.3.1:** Nyquist plot for a typical impedance curve of a commercial LIB. The imaginary part of impedance is plotted against the real part of impedance. The plot is divided into three regions, high frequency (HF), mid frequency (MF) and low frequency (LF). Figure from[27].

tracted, the intercept with the real axis in the high-frequency region, observable in Figure 2.3.1, corresponds to the sum of internal ohmic resistances in the electrolyte, active materials, current collectors and metal contacts of the battery. At this frequency only electrons are fast enough to move. This region is defined as the frequency domain above 1 kHz. The middle frequency region, with frequencies of 1 Hz to 1 kHz, arcs in the Nyquist plot are primarily due to processes occurring at interfaces between electrodes and the electrolyte. The processes have both capacitive and resistive impedance related to them. For LIBs, due to the inherent instability of the electrolyte in contact with the electrodes, SEIs are created where the electrolyte is decomposed at the electrodes. These layers result in arcs in the Nyquist plot because $Li^+$ must be transported through them during charging and discharging. Simultaneously with the ion transport,

dielectric polarisation occurs from the electric field. As ions are intercalated into the electrode particles, double layer charging happens in parallel. Therefore, there are charge transfer and SEI transport on both electrodes contributing to the impedance in the middle-frequency region of the Nyquist plot. For the low-frequency region of the plot, mainly diffusion related processes contribute to the impedance.

Due to the two electrode EIS measurements being utilised in this master's thesis, it can be difficult to distinguish between processes occurring at the cathode and processes occurring at the anode. The problem arises if the processes at the two electrodes have similar time constants, resulting in combined arcs in the mid-frequency region of the Nyquist plot. Implementing a third reference electrode could help to deconvolute the contributions from the different processes, but it can affect the battery cell performance. Therefore, interpretation of the data acquired must be done carefully.

For interpreting the impedance data, different methods are being utilised. The most common method is to model the battery cell and the different physical processes occurring as an electrical circuit with each process presented as a circuit element. The method is called Equivalent Circuit Modelling (ECM) and gives rapid and broad insights into the battery cell performance. However, without proper knowledge of the battery, it is easy to overparameterise to get a good data fit and end up having circuit elements that does not describe any physical process happening inside the battery cell. Therefore, the best practice is to minimise the number of circuit elements in the ECM, where each element can describe a physical process.

Circuit elements for the high frequency region is usually an inductor in parallel with a resistor to model the wiring, in series with a resistor to model the ohmic resistance in the electrolyte and electrodes. For the mid-frequency region two resistor capacitor parallels are connected in series to model the SEI-layer and the charge-transfer. For the low frequency region the diffusion process is modelled with a Warburg element, usually in series with the charge-transfer resistor. Figure 2.3.2 shows the circuit diagram for the ECM of the above-described circuit.

To better fit the experimental values, capacitor elements are replaced with constant phase elements (CPEs). Several theories have been proposed to explain the nature of imperfect capacitor behaviour. Electrode surface roughness, distribution of reaction rates, varying coating thickness and non-uniform current distribution are examples[36]. It is parameterised by a quantity Q with a phase angle $\alpha$ and the impedance is calcu-
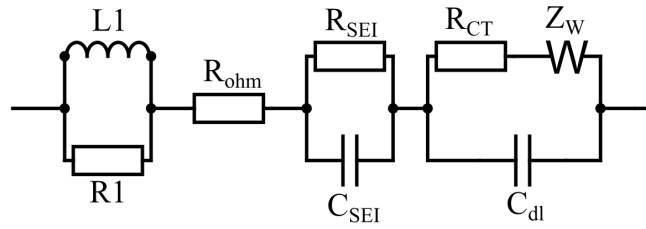
**Figure 2.3.2:** Equivalent Circuit Model example for one side of a LIB. L1‖R1 represents the wiring inductance and resistance, respectively, while $R_{ohm}$ represents the ohmic resistance in the electrolyte and electrode. $R_{SEI}‖C_{SEI}$ represents ion transport and dielectric polarisation at the SEI, respectively. $R_{CT}‖C_{dl}$ represents the charge transfer and double layer charging/discharging at the electrode, respectively. $Z_W$ represents the diffusion process in the electrode.

lated

$$Z_Q^* = \frac{1}{Q(j\omega)^\alpha} \tag{2.3.2}$$

where the phase angle is between 0.5 and 1. CPEs should be treated carefully, since capacitive effects differing by orders of magnitude may fit the experimental data by altering the phase angle [27].

A generic ECM (from high to low frequency) for an SSB with Li anode consists of a bulk RC parallel in series with a grain boundary RC parallel at HF, in series with an anode interface RC parallel in series with a cathode interface RC parallel at MF, in series with a CPE or Warburg element to represent the diffusion processes in the electrodes at LF. The CPE element is for a more capacitive behaviour in the LF region. It is important to be aware of differences between SSBs, because the impedance curves varies from system to system. In Figure 2.3.3, the anode interface resistance was attributed to the LF semicircle, opposite of the generic ECM utilised for SSBs with a Li anode. The bulk resistance was also represented by a single resistor, instead of an RC parallel.
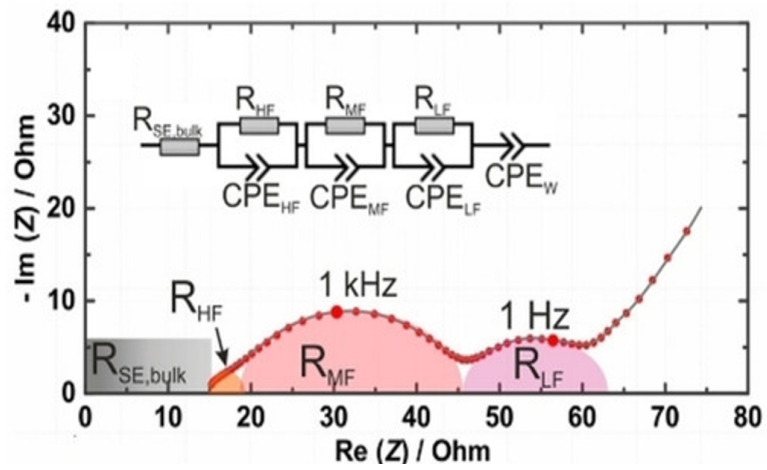
**Figure 2.3.3:** Nyquist plot for an In|LGPS|LCO cell. The contributions are divided into HF, MF and LF. Figure from [42].

# Chapter 3

# Experimental

## 3.1 Mechanochemical synthesis of LYC-nanoparticles

During the specialisation project, $Li_3YCl_6$ powders were synthesised by a mechanochemical scheme, utilising LiCl and $YCl_3$ in a stoichiometric ratio. After 132 hours of milling, half of the powder was added to one ball-milling container and the other half to the other ball-milling container. In an attempt to react more of the leftover LiCl, approximately 10 mg of $YCl_3$ powder was added to one of the containers before milling for a final 22 hours. The two containers will be referred to as "LYC w/o Y" and "LYC w/ Y" for the $Li_3YCl_6$ powder that did not receive additional $YCl_3$ before ball-milling the last 22 hours and the $Li_3YCl_6$ powder that did receive additional $YCl_3$, respectively.

Rietveld refinement was performed for "LYC w/ Y" by utilising the Bruker Topas software to determine phase purity and crystal size. Table 3.1.1 shows site information of the Rietveld refinement.

**Li$_3$YCl$_6$ - mechanochemical synthesis, Phase purity = 91.1(8) wt%**

**Lattice parameters:** $a$ = 11.240(3), $c$ = 6.0490(19)

**R$_{wp}$ = 4.28, R$_{exp}$ = 3.72, Space group = *P-3m1***

| Atom | Wyckoff position | $x$ | $y$ | $z$ | Occ. | $B_{iso}$ |
|---|---|---|---|---|---|---|
| Y | 1*a* | 0 | 0 | 0 | 1 | 3.1(3) |
| Y | 2*d* | 0.33333 | 0.66667 | -0.044(7) | 0.54(2) | 3.1(3) |
| Y | 2*d* | 0.33333 | 0.66667 | 0.534(9) | 0.46(2) | 3.1(3) |
| Cl | 6*i* | 0.2153(12) | 0.7847(12) | 0.288(3) | 1 | 0.14(18) |
| Cl | 6*i* | 0.5543(16) | 0.4457(16) | 0.285(3) | 1 | 0.14(18) |
| Cl | 6*i* | 0.89997(9) | 0.1003(9) | 0.259(5) | 1 | 0.14(18) |
| Li | 6*g* | 0.2884 | 0 | 0.5 | 0.5 | 1 |
| Li | 6*h* | 0.3397 | 0 | 0 | 1 | 1 |

**Table 3.1.1:** Rietveld-refinement results of X-ray diffraction data for mechanochemically synthesised Li$_3$YCl$_6$ with added YCl$_3$.

## 3.2 Mechanofusion of Li$_3$YCl$_6$ solid electrolyte on NCA particles

10.0 g pre-mechanofused NCA powder was mixed with 0.310 g LYC by VWR analog vortex mixer for 1 minute. The vial was transferred to the glove box containing the Picobond mechanofusion machine in the Picoline series by Hosokawa company. The powder was poured into the chamber of the mechanofusion machine and the lid was closed. The machine ran at 3600 rpm for 1 hour before the chamber was opened and the powder retrieved.

7.28 g pristine NCA powder was mixed with 0.111 g LYC by hand grinding utilising pestle and mortar for 15 minutes. The mixed powder was put in a vial and sealed. The vial was transferred to the glove box containing the Picobond and similarly the powder was poured into the chamber and lid closed. The machine ran at 3600 rpm for 1 hour. After finishing, the powder was retrieved from the chamber.

An image of the mechanofusion machine inside a nitrogen filled glove box can be observed in Figure 3.2.1. The glove box was necessary to protect LYC from reacting with any moisture inside the lab.



|         (a)         |         (b)         |
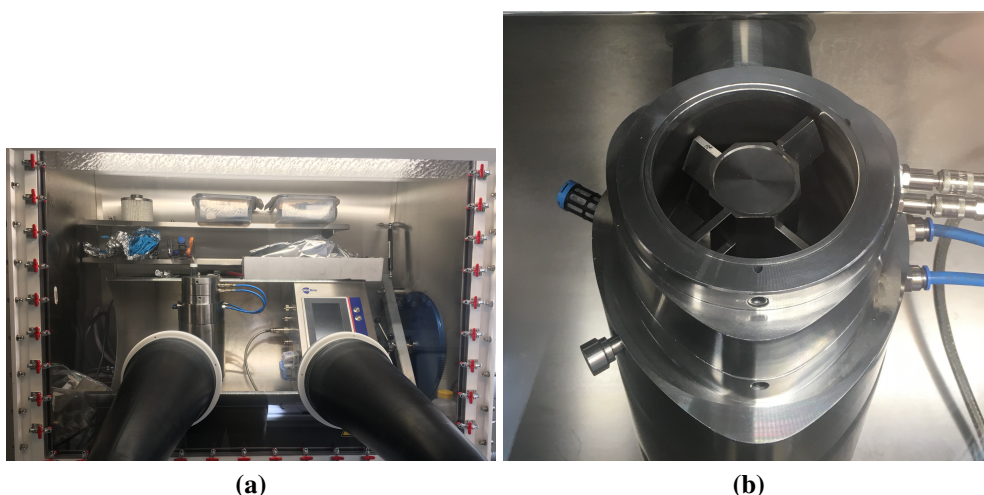
**Figure 3.2.1:** Picobond mechanofusion machine in the Picoline series inside a N$_2$-filled glove box. (a) glove box with Picobond inside. (b) Close-up of Picobond chamber.

### 3.2.1   Electron microscopy imaging and elemental mapping of coated particles

Two samples were prepared for FIB-SEM and TEM with energy-dispersive X-ray spectroscopy (EDS). The two LYC-coated NCA samples were pressed onto aluminium foil substrates inside a glove box ($H_2O < 2$ ppm, $O_2 < 4$ ppm). They were inserted into a FEI Helios G2 FIB/SEM instrument. Lamellae from large ( 20 μm) round particles were extracted and attached to a Cu TEM half-grid. The surface regions of the particles were thinned to about 100 nm utilising the 30 kV $Ga^{2+}$ beam. The final thinning was done with 5 kV ions to reduce ion implantation and surface amorphisation. From the extraction from the glove box to the insertion into the TEM, the samples were exposed to air for a total of about 20 min.

TEM and STEM imaging was done utilising a JEOL JEM-2100F microscope operated at 200 kV. An annular dark-field (ADF) detector was utilised for STEM imaging, giving mass density / thickness contrast. An Oxford X-MAX 80T detector was utilised for EDS. The characteristic $K\alpha$ peaks were mapped for all elements present.

## 3.3 Conventional coin cell fabrication and electrochemical testing

Coin cells utilising pristine NCA cathode powder were fabricated and compared electrochemically with the LYC-coated NCA powders. The following subsections describe the process of preparing the necessary components for coin cell fabrication, the fabrication itself and the electrochemical testing procedures utilised to compare the cell chemistries.

### 3.3.1 Binder solution and slurry preparation

Polyvinylidene fluoride (PVDF, Sigma-Aldrich) dissolved in N-Methyl-2-pyrrolidone (NMP, Sigma-Aldrich, 99.5%) was utilised for cathode fabrication. 2.0043 g PVDF was mixed with 38.0013 g NMP to create a 40.0173 g solution of 5.009 wt% PVDF in NMP. The solution was stirred at 150 rpm at room temperature for two days to ensure a homogeneous solution.

Carbon Super C65 (C65, Sigma-Aldrich, 99.95%) and NCA (Sigma-Aldrich, >98%) was added to a glass vial and dry mixed utilising VWR analog vortex mixer at 3000 rpm for 1 minute. C65, NCA, PVDF-solution and NMP was added to stainless steel containers. The amount of NCA, C65 and PVDF for the cathode should be approximately 90%, 5%, 5% respectively for the reference cells. For the coated NCA particles, the active material will be slightly lower, but the amount of C65 and PVDF remains the same. LYC-coated NCA powder with 3 wt% and 1.5 wt% LYC was utilised for 2505_NCA_3 and 2505_NCA_1.5, respectively. Table 3.3.1 shows the three NCA slurry mixes that were utilised for coin cell fabrication and GCPL measurements.

| Slurry mix | NCA / g | C65 / g | PVDF-sol / g | PVDF / g | NMP / g |
|------------|---------|---------|--------------|----------|---------|
| 2102_NCA | 2.2620 | 0.1297 | 2.4773 | 0.1239 | ∼1 |
| 2505_NCA_3 | 0.8996 | 0.0501 | 0.9913 | 0.0496 | 0.5053 |
| 2505_NCA_1.5 | 0.9003 | 0.0506 | 1.0060 | 0.0503 | 0.5333 |

**Table 3.3.1:** Slurry mixes utilised for cell assembly of NCA reference cells and LYC-coated NCA cells.

### 3.3.2 Cathode fabrication

Different equipment utilised for electrode fabrication is pictured in Figure 3.3.1.

Table 3.3.2 shows the fabrication scheme for 2102_NCA. Calendering was performed
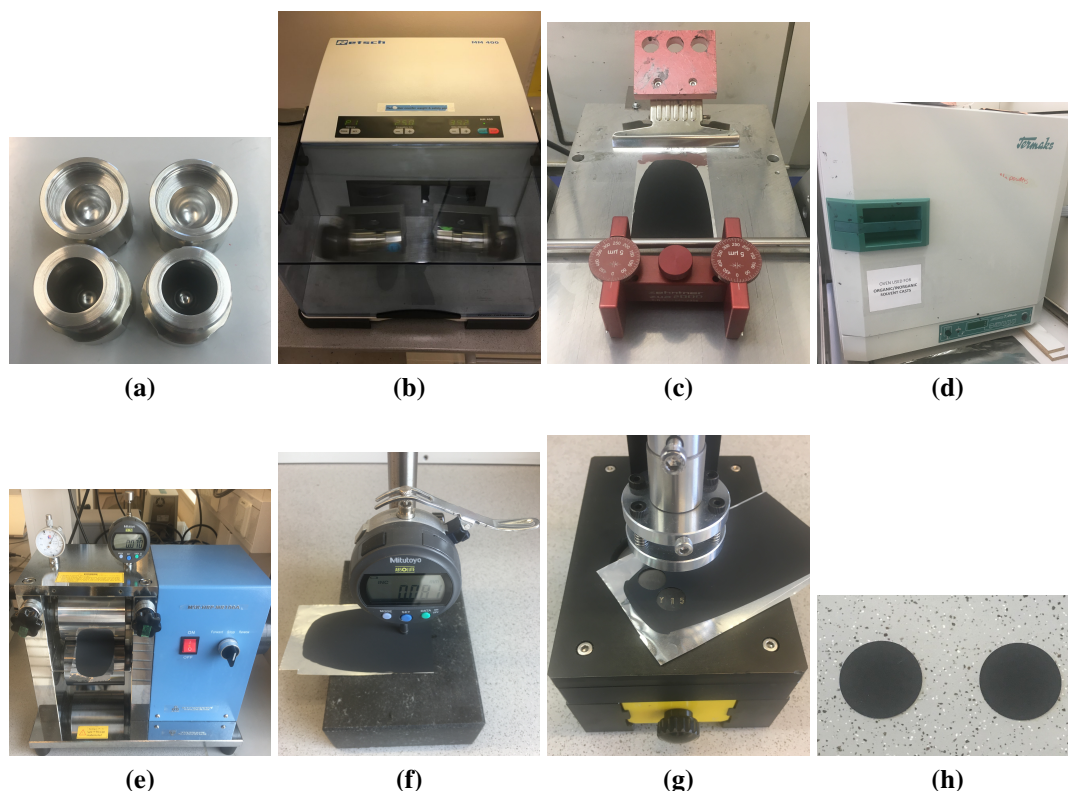
**Figure 3.3.1:** Electrode fabrication equipment. (a) Stainless steel slurry containers utilised with Retsch MM400. (b) Retsch MM400 slurry mixing machine. (c) RK control casting machine and doctor blade. (d) Termaks convection oven. (e) MSK-HRP-MR100A calendering machine. (f) Mitutoyo absolute for measuring electrode thickness before and after calendering. (g) Gelon manual punching machine. (h) 14 mm diameter cut electrodes.

in a forward and reverse direction. All dried electrode casts were cut into 14 mm diameter discs utilising a Gelon GN-CP20 manual punching machine. The electrodes were weighed utilising a Sartorius MSA225P-100-DU lab scale.

| Production Scheme 2102_NCA | | | | | |
|---|---|---|---|---|---|
| **Type** | **Instrument** | **Gap / μm** | **T / °C** | **Time** | **Freq. / Hz** |
| Mixing | Retsch MM400 | | RT | 10 + 45 min | 10 + 25 |
| Casting | Doctor blade | 250 | RT | 10 min | |
| Drying | Convection oven | | 80 | 42 h | |
| Calendering | MSK-MR100A | 80 | RT | | |
| Moisture | Vacuum drying | | 120 | 18 h | |

**Table 3.3.2:** Production scheme of 2102_NCA electrodes

Table 3.3.3 shows the production scheme for the 3 wt% LYC-coated NCA electrodes and the 1.5 wt% LYC-coated NCA electrodes. Due to the air sensitivity of LYC, all fabrication steps were performed inside an Ar-filled glove box ($H_2O \leq 0.1$, $O_2 \leq 2.0$),

except slurry mixing, since the stainless steel containers were filled with slurry inside the glove box and kept air tight. Due to no available convection oven inside any glove box, drying was performed by utilising hot plates inside the glove box. Attempts were made to compress electrodes with a hydraulic press inside the glove box, however it did not reduce the thickness of the cast. Cells assembled with these electrodes were as a result not calendered.

| Production Scheme 2505_NCA_3 and 2505_NCA_1.5 | | | | | |
|---|---|---|---|---|---|
| Type | Instrument | Gap / μm | T / °C | Time | Freq. / Hz |
| Mixing | Retsch MM400 | | RT | 10 + 45 min | 10 + 25 |
| Casting | Doctor blade | 250 | RT | 10 min | |
| Drying | LLG unistirrer 3 | | 50 | 14 h | |

**Table 3.3.3:** Production scheme of 2505_NCA_3 and 2505_NCA_1.5 electrodes.

### 3.3.3 Coin cell fabrication

Figure 3.3.2 shows an exploded view drawing of a 2032 coin cell assembly, naturally starting with the bottom cap. 10 μL 1 M $LiPF_6$ (Sigma Aldrich, battery grade) in 1:1 ethylene carbonate (EC, Sigma Aldrich, battery grade) : diethyl carbonate (DEC, Sigma Aldrich, battery grade) electrolyte was utilised to stick the 14 mm cathode foil to the middle of the large cap. 20 μL electrolye was utilised to wet the cathode. The separator was then placed on top. An additional 20 μL electrolyte was added to wet the separator. The gasket for the small cap was then placed in the large cap. A 15.6 mm Li disc was placed on the wetted separator. A stainless steel 1 mm thick disc was placed on the lithium with a wave spring on top. Lastly, the small cap was placed on the spring to close the cell. The cells were crimped for 3 seconds utilising a Hohsen Automatic Coin Cell Crimper. The complete process was performed inside an Ar-filled glove box ($H_2O$ and $O_2 \leq 0.1$ ppm).

### 3.3.4 Electrochemical testing

After crimping, coin cells were left to rest for 12 hours before cycling to let the electrodes be properly wetted by the electrolyte. Longterm cycling was performed with two formation cycles at 0.1C charge/discharge rate, with a voltage range of 2.75 - 4.3 V (vs Li/Li$^+$). After the formation cycles, the cells were cycled at a 1C rate for 100 cycles at 25±1 °C with a voltage range of 2.75 - 4.3 V (vs Li/Li$^+$). GCPL with a constant current/constant voltage (CCCV) charging setup, was utilised. After charging to 4.3
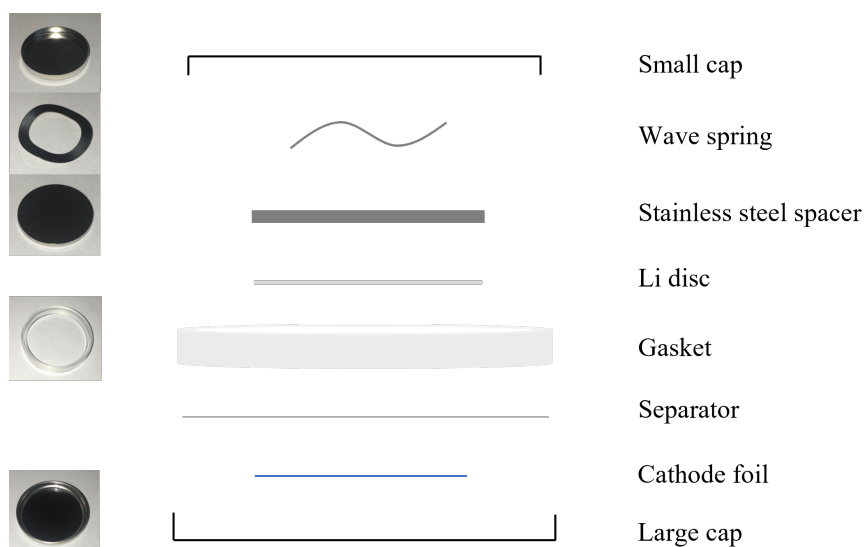
**Figure 3.3.2:** Exploded view of an assembled coin cell with description of the different coin cell parts. Pictures are included of metal parts and the gasket.

V, the cell voltage was kept constant until either the current dropped off to 0.05C or 2 hours had passed. After the constant voltage step, the discharging step was initialised with constant current discharging until the lower cut-off voltage was reached. Cycling was performed utilising a VMP-300 Biologic potensiostat. EIS measurements were performed before cycling and after the 100th cycle from 10 kHz to 10 mHz.

## 3.4 SSB fabrication and electrochemical testing

SSBs utilising pristine NCA powder and LYC-coated NCA powders were fabricated. The first subsection describes the process of SE pellet fabrication and the conductivity measurement of those. The second section describes the process of making the Li-In alloy for the SSBs. The third section describes the fabrication and electrochemical testing of the SSBs utilising pristine and coated NCA cathodes, as well as EIS measurements of the cells.

### 3.4.1 Conductivity measurement of LPSC and LYC

Polyether ether ketone (PEEK)-cells were utilised for both pressing the LPSC-pellet and performing the EIS measurements for determining the ionic conductivity of the electrolyte. The PEEK cell consists of the PEEK-casing, two plungers and two gold sputtered spacers. The shorter plunger was placed in the bottom of the PEEK-casing and one of the gold sputtered spacers was inserted into the 10 mm diameter hole. 70 mg of LPSC was then poured in and lightly compressed by the longer plunger. The other disc was placed on top of the LPSC-pellet. The pellet was pressed with approx. 250 MPa pressure and kept at this pressure while doing the EIS measurement from 1 MHz to 100 mHz. The measurement was performed with a Modulab XM Solartron potensiostat. The thickness of the pellet was measured by a caliper with digital display to be $0.39 \pm 0.005$mm. The conductivity was calculated by utilising Equation 2.2.2 to formulate

$$\sigma = \frac{l}{RA},$$ (3.4.1)

where l is the pellet thickness, A the pellet cross-section and R the bulk resistance determined by EIS.

The LYC-pellet was fabricated similarly to the LPSC-pellet. EIS was measured while the pellet was under a 250 MPa pressure. The measurement was from 7 MHz to 100 mHz and was performed with a VMP-300 Biologic potensiostat. The pellet thickness was measured to be $0.79 \pm 0.005$mm.

### 3.4.2 Li-In alloy fabrication

Li-In alloys were made by lithiation of In foil in coin cells. 2032 coin cells were assembled by placing a 10 mm In foil on a stainless steel spacer with a 25 μm thick, 19 mm Celgard separator. 10 μL electrolyte of 1 M lithium bis (trifluoromethanesul-

fonyl)imide (LiTFSI, Gelon) dissolved in dioxolane (DOL, Gelon) and dimethoxyethane (DME, Gelon) with a 1:1 ratio was added. A 15.4 mm Li disc was utilised as the other electrode with another stainless steel disc on top. The coin cell was crimped for 5 seconds utilising a Hohsen Corporation automatic coin cell crimper.

The plating process was done by discharging the cell at a current density of $0.1\,\mathrm{mA\,cm^{-2}}$, utilising 10 second discharge, 10 second rest cycles for 6 hours. To retrieve the lithiated In foil attached to the stainless steel spacer, the cell was disassembled by utilising the Hohsen Corporation coin cell disassembler tool. After retrieving the lithiated In foils, they were washed with DME (Sigma Aldrich, >99%) for 5 minutes and dried inside an oven for 2 hours at 50 °C inside a glove box ($H_2O \leq 0.1$ ppm, $O_2 \leq 0.5$ ppm).

### 3.4.3  SSB fabrication and electrochemical testing

Solid-state NCA half cells consisting of NCA composite, LPSC (NEI corporation) SE and Li-In alloy were fabricated in the following procedure: 90 mg LPSC was poured into a PEEK cell. The powder was pressed at 375 MPa pressure for 3 minutes. NCA:LPSC:C65 composite powder (11:16:1 by weight) was mixed by pestle and mortar for approx. 15 minutes. The short plunger was removed and 12 mg was poured on the flat SE pellet. The powders were pressed at 375 MPa pressure for 3 minutes. The long plunger was removed and the Li-In alloy was inserted. The cell was pressed at 150 MPa pressure for 1 minute.

A similar procedure was selected for the SSB cells utilising coated NCA powder. Approximately 12 mg coated NCA:LPSC:C65 (11:16:1 by weight) was used as cathode composite. Due to the coating material for the coated NCA, the amount of active material in the cell was approx. 4.64 g for the 1.5 wt% LYC-coated NCA and 4.57 g for the 3 wt% LYC-coated NCA.

Table 3.4.1 shows the approx. stack pressures for the different reference cells and cells with coated NCA cathodes. The cells were held under constant pressure by two steel plates, tightened by nuts and three bolts connecting the bottom and top steel plate. A torque wrench set to 2.5 N m was utilised to tighten the nuts for the top plate. Each setup was tested with a force sensor and the load utilising 2.5 N m for the three nuts was measured. Before cycling, the force sensor was removed and the setups were tightened with 2.5 N m torque again. Figure 3.4.1(a) shows the setup, here connected to a potensiostat.

| Cell name | Cell type | Stack pressure / MPa |
|---|---|---|
| 6_mg_load_HC_2 | Uncoated | 56 |
| 6_mg_load_HC_3 | 3 wt% LYC | 60 |
| 6_mg_load_HC_4 | Uncoated | 60 |
| 6_mg_load_HC_5 | Uncoated | 58 |
| 6_mg_load_HC_6 | 1.5 wt% LYC | 61 |
| 6_mg_load_HC_7 | 1.5 wt% LYC | 63 |
| 6_mg_load_HC_8 | 3 wt% LYC | 70 |
| 6_mg_load_HC_9 | 3 wt% LYC | 56 |
| 6_mg_load_HC_10 | 1.5 wt% LYC | 56 |

**Table 3.4.1:** Table showing the different cells, their cell type and the approximate stack pressures during GCPL measurements and EIS.



**(a)**  **(b)**
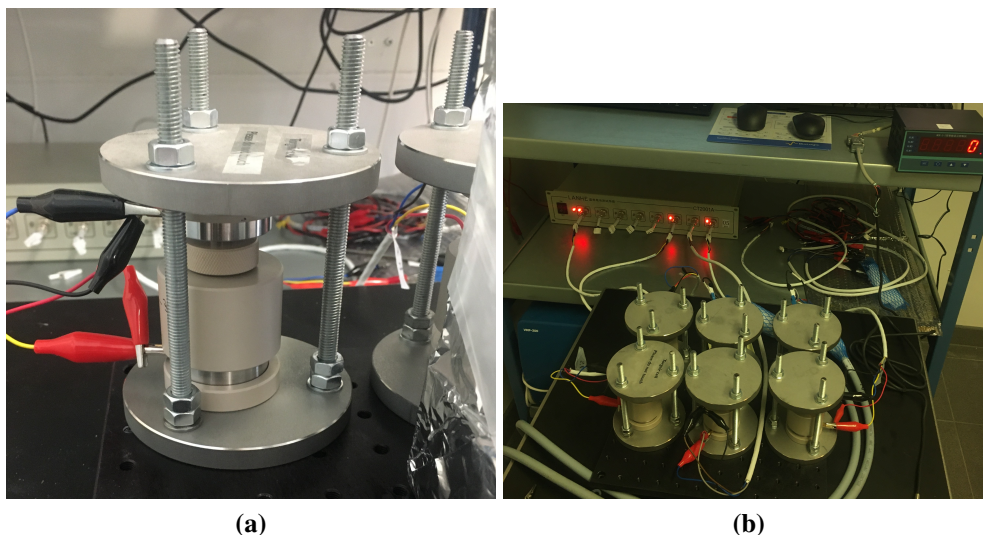
**Figure 3.4.1:** Battery cell setup during cycling and EIS measurements. (a) Close-up of the PEEK cell being held under constant pressure by the steel cage. (b) The cells were placed on a plate that resists vibrations from the pump utilised for the large glove box inside the lab. The force sensor is visible in the background to the top right.

The cells were cycled at 2.178 - 3.678 V (vs. Li-In/Li$^+$) with a C-rate of 0.1C. The average temperature during cycling was 24±1°C. The batteries were cycled on an anti-vibration plate due to issues with nuts loosening inside the lab for the first attempted SSBs. The cycling setup inside the lab is shown in Figure 3.4.1(b).

# Chapter 4

# Results

## 4.1 Synthesis of the coating material

Two powders were obtained after ball-milling for a total of 154 hours at 600 rpm during the specialisation project. "LYC w/ Y" achieved a phase-purity of approximately 91.1 wt% and an average crystal size of 17.5 nm. Figure 4.1.1 shows the "LYC w/ Y" XRD raw data points and the calculated pattern from Rietveld refinement with the parameters given in Table 3.1.1. Most of the difference can be attributed to background noise, but a notable difference between the raw data and calculated pattern can be observed for the peak at 48.8 ° $2\theta$.
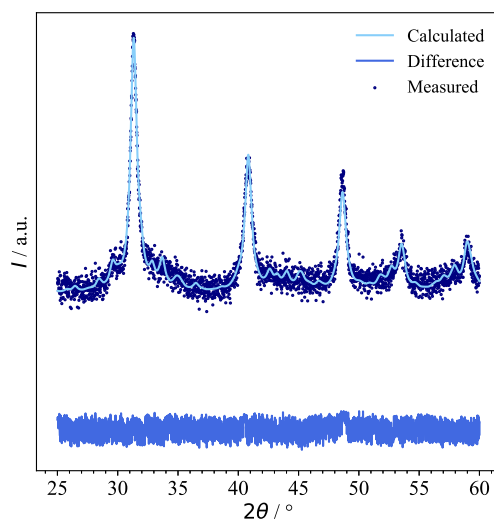


**Figure 4.1.1:** Measured and calculated data from Rietveld analysis.

## 4.2 Dry-coating of NCA particles by mechanofusion

SEM images were taken of pristine and mechanofused NCA particles as depicted in Figure 4.2.1 and Figure 4.2.2, respectively. This was done to observe differences in morphology, since those could affect the later coating process. From the overview im-
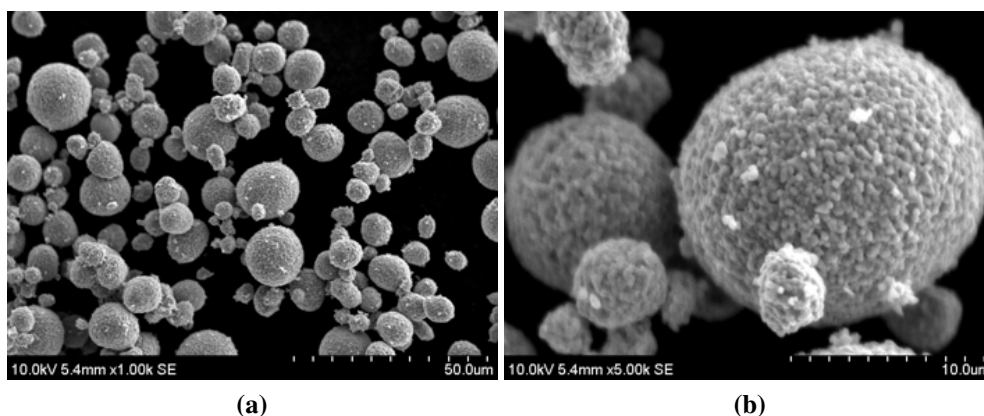


**Figure 4.2.1:** SEM images of pristine NCA particles. (a) Overview. (b) Close-up of a secondary particle.
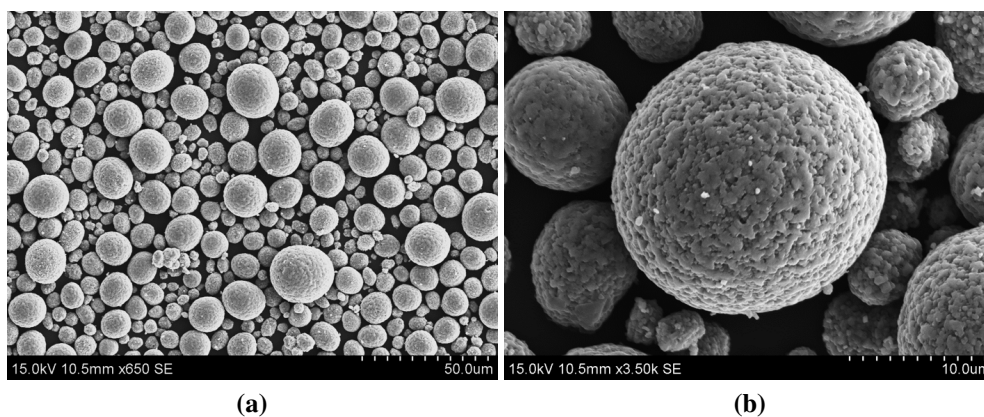


**Figure 4.2.2:** SEM images of mechanofused NCA particles. (a) Overview. (b) Close-up of a secondary particle.

ages in Figure 4.2.1(a) and Figure 4.2.2(a), it seems that the mechanofused secondary particles are slightly rounder and has smoother surfaces. To confirm the difference in smoothness, close-up images were taken of a pristine and a mechanofused secondary particle in Figure 4.2.1(b) and 4.2.2(b), respectively. For the pristine secondary particle there are pronounced primary particles on the surface. From the image scale, it looks like the primary particles are approximately 1 μm in diameter, on average. The mechanofused secondary particle shows a smoother surface with less defined primary

particles. However, the surface still has some degree of roughness, with visible darker spots between the primary particles. It also looks like the primary particles are slightly wider, likely due to the deformation of the surface, which will be discussed in Section 5.1.

When retrieving the 3 wt% LYC-coated NCA powder after mechanofusion, some LYC particles could still be observed. The agglomerated particles were likely not broken down during mechanofusion and due to their size, could not attach to the surface of NCA secondary particles. To make sure most of the LYC particles would be coated for the 1.5 wt% LYC coating, the more rigorous mixing procedure with pestle and mortar was selected. The pestle and mortar mixing seemed to work as no LYC particles were visible after mechanofusion.

SEM images were taken of the 1.5 wt% coated NCA secondary particles to study the surface coverage and morphology of the coating material, depicted in Figure 4.2.3(a). The surface looks smoother than the pristine NCA in Figure 4.2.1(b), but rougher than the mechanofused NCA in Figure 4.2.2(b). To better see the uniformity and thickness of the coating, a cross section was made and a FIB-SEM image taken, seen in Figure 4.2.3(b). It shows the primary particles of a secondary particle. At the interface between the dark Pt layer and the surface of the secondary particle, there is a brighter phase. It is thickest in the highlighted region, a few hundred nanometers thick. This is likely the LYC coating. The coating seems uneven and in some places it is not visible, suggesting either a very thin or missing coating. For further analysis with STEM and EDS, a FIB-lamella was cut of the secondary particle, depicted in Figure 4.2.3(c).



**(a)** **(b)** **(c)**
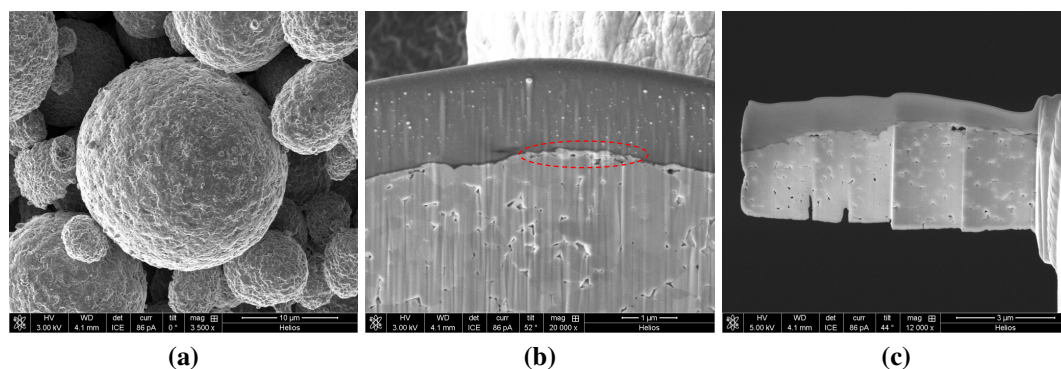
**Figure 4.2.3:** SEM images of NCA coated by 1.5 wt% LYC. (a) NCA secondary particle surface. (b) Cross-section of a coated NCA secondary particle. In highlight: coating layer, a few hundred nanometers thick. (c) Fib-lamella of an NCA secondary particle.

Similarly, SEM images were taken of the 3 wt% coated NCA secondary particles to
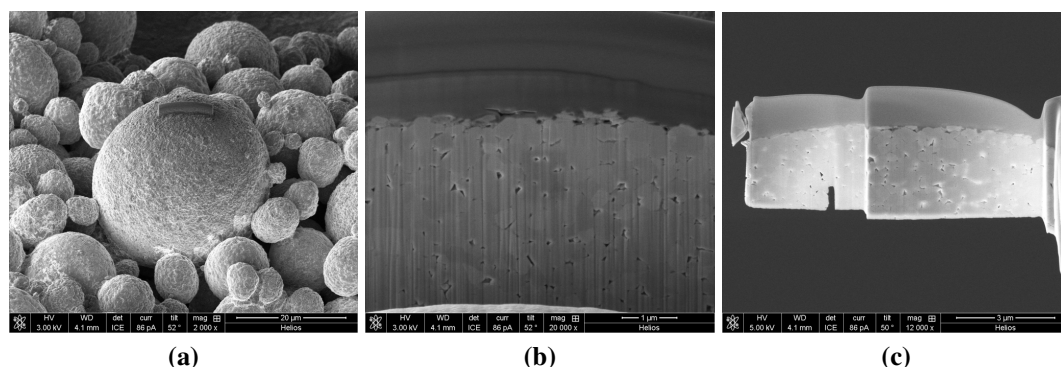


**Figure 4.2.4:** SEM images of NCA coated by 3 wt% LYC. (a) NCA secondary particle surface. (b) Cross-section of a coated NCA secondary particle. (c) Fib-lamella of an NCA secondary particle.

study the coating surface coverage and morphology, depicted in Figure 4.2.4(a). The surface is clearly rougher than the 1.5 wt% coated NCA, but the degree of surface coverage is hard to tell. The FIB-SEM image in Figure 4.2.4(b) does not provide information about any coating, unlike for the 1.5 wt% image. It does however still show the primary particles of the NCA secondary particle. A FIB-lamella was prepared for STEM and EDS to provide information about any potential coating, depicted in Figure 4.2.4(c).

In the STEM image in Figure 4.2.5, inside the map area used for EDS, coating is
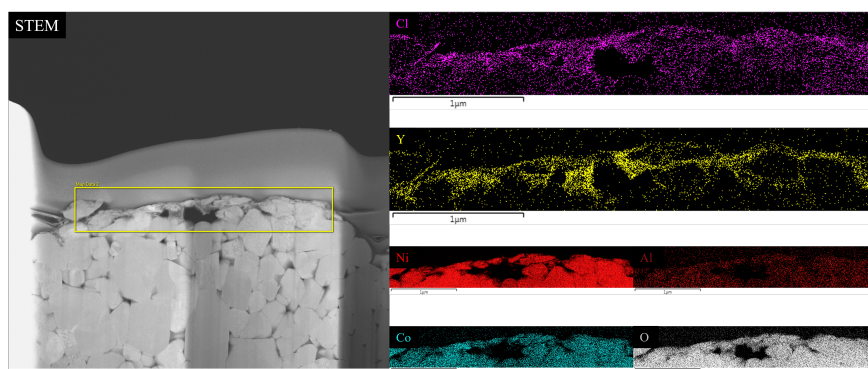


**Figure 4.2.5:** STEM image with element mapping of 1.5 wt% LYC-coated NCA lamella.

visible with what looks like smaller particles than the primary particles of NCA. The coating thickness seems to be uneven. EDS was performed to confirm whether the coating was LYC or not. A clear presence of Y and Cl in the coating indicates that it is most likely LYC. The presence of NCA-related atoms in the coating could be explained by the ion milling process, probably causing some scattering of the atoms.

The STEM image in Figure 4.2.6 provides some of the desired information that was not visible with SEM. A porous coating, approximately 20 nm thick, can be observed as a bright layer in the left part of the image. EDS shows the presence of Y and Cl in yellow and magenta, respectively, to confirm that the coating is of the LYC material. It looks like a thin and homogeneous coating, with only a few nm variation in thickness. The same presence of the NCA-related atoms in the coating as for the 1.5 wt% coating can be seen here.
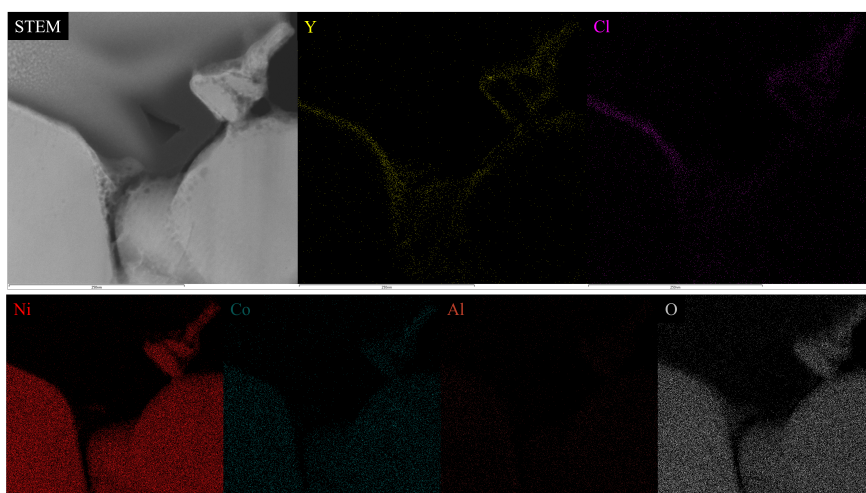


**Figure 4.2.6:** STEM image with element mapping of 3 wt% LYC-coated NCA lamella.

## 4.3 Conventional coin cell testing

In this section, coin cells with conventional liquid electrolyte were evaluated by electrochemical tests and EIS. The tests were performed with three cells for each test to obtain better and more accurate statistics for the results presented in this thesis. This in turn not only provides a better understanding of the effect of external cell fabrication parameters on the battery performance, but also ensures the reproducibility of the results.

The coin cells were charged and discharged at 1C for 100 cycles with a voltage range of 2.75 - 4.3 V (vs Li/Li$^+$). The discharge capacity of the different cell types is important because it measures how much useful charge the battery is able to deliver for its given weight. The CE is important, because it gives information about how much useful charge the cell is able to deliver for a given charge it has consumed.
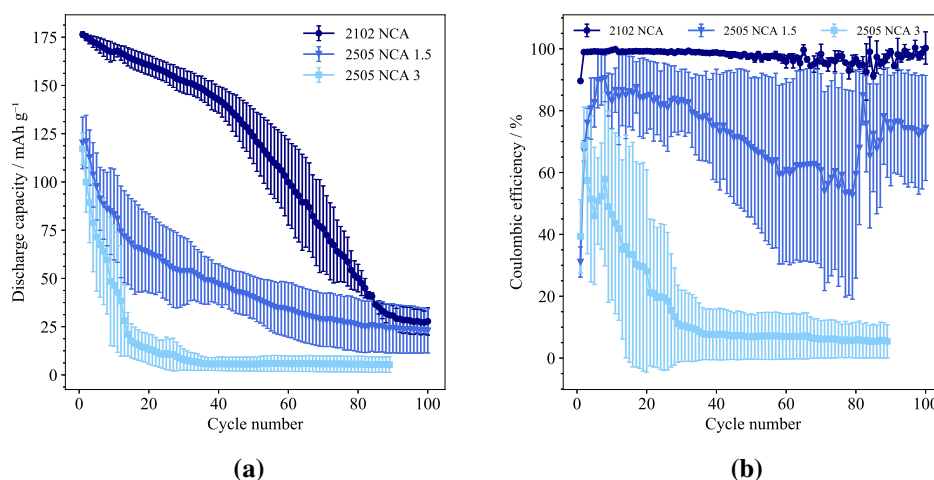


**Figure 4.3.1:** Cycling performance of coin cells with pristine and coated NCA cathodes cycled at 1C and voltage range of 2.75 - 4.3 V (vs Li/Li$^+$). 2102 NCA in navy, 2505 NCA 1.5 in royalblue and 2505 NCA 3 in lightskyblue. (a) Discharge capacity versus cycle number and (b) CE versus cycle number for the same battery cells.

Information about the discharge capacity and CE of the coin cells during cycling is given in Figure 4.3.1. In the figure, the cells with pristine NCA was given the name 2102 NCA, which is the same as in Experimental, while NCA coated with 1.5 wt% LYC was named 2505 NCA 1.5 and NCA coated with 3 wt% LYC was named 2505 NCA 3. From the beginning, a significant difference in the average discharge capacities can be observed in Figure 4.3.1(a). The 2102 NCA cells show an average initial

discharge capacity of 176.4 $\mathrm{mAhg^{-1}}$, while the 2505 NCA 1.5 and 2505 NCA 3 cells show average initial discharge capacities of 120.2 $\mathrm{mAhg^{-1}}$ and 117.2 $\mathrm{mAhg^{-1}}$, respectively. Following the initial cycle, the capacity fade is quite rapid, especially for the 2505 NCA 3 cells. At around cycle 45, something causes the NCA 2102 cells to gain accelerated capacity fade.

Similar to the low discharge capacity of the coated cells, the CE is also poor, as shown in Figure 4.3.1(b). For the 2102 NCA cells, the initial Coulombic Efficiency (ICE) was 89.6% and they remained a relatively stable CE of 97.7% for the 100 cycles. In contrast, the 2505 NCA 1.5 cells achieved an ICE of only 31.1%, although the CE increases the first 10 cycles before it decreases until about cycle 80 and stabilises towards cycle 100. For the 2505 NCA 3 cells, the ICE was 39.4%, then jumped to 68.8% before it decreased rapidly to below the ICE value.

The trends in Figure 4.3.1 could correlate with the internal resistance of the cells, therefore EIS measurements were performed before and after cycling to see how it had changed. Figure 4.3.2 shows the EIS measurements of the pristine and coated cells as Nyquist plots with ECMs. In Figure 4.3.2(a) the ECM consists of solution resistance (electrolyte and separator) $R_s$, charge-transfer resistance $R_{ct}$, double-layer capacitance $CPE_{dl}$ and blocking electrode $CPE_{be}$. A larger solution resistance is visible for the coated cells compared to the pristine cell, but the opposite is true for the charge-transfer resistance. During the first cycle, SEI formation takes place and therefore a second semicircle becomes visible in Figure 4.3.2(b). The ECM utilised now consists of solution resistance $R_s$, SEI resistance $R_{SEI}$, SEI capacitance $CPE_{SEI}$, charge-transfer resistance $R_{ct}$ and double-layer capacitance $CPE_{dl}$. After charging, a moderate and similar increase in solution resistance can be seen for all cell types. The SEI resistance is largest for the 2505 NCA 1.5 cell and smallest for the pristine NCA cell. Furthermore, a small increase in charge-transfer resistance can be seen for the 2505 NCA 1.5 cell, while it increased substantially for the other two.

The quantities for the resistances before and after cycling in Figure 4.3.2 can be seen in Table 4.3.1.

**(a)**        **(b)**
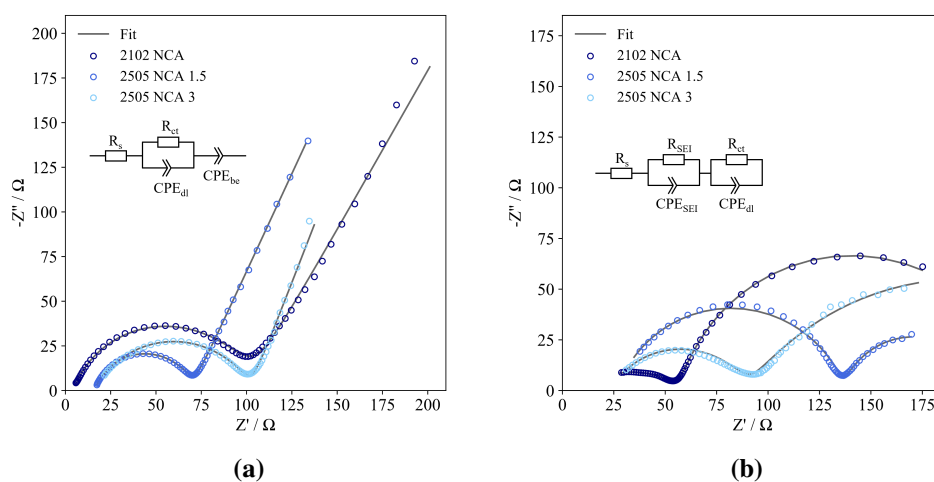
**Figure 4.3.2:** Nyquist plot from 10 kHz to 100 mHz of the coin cells with pristine and coated NCA cathodes. Coloured markers are experimental values, while lines are ECM fits. 2102 NCA in navy, 2505 NCA 1.5 in royalblue and 2505 NCA 3 in lightskyblue. (a) Impedance data before cycling. (b) Impedance data after 100 cycles.

| Cell | 2102 NCA | | 2505 NCA 1.5 | | 2505 NCA 3 | |
|---|---|---|---|---|---|---|
| Cycling | Before | After | Before | After | Before | After |
| $R_s$ [$\Omega$] | 4.4 | 8.4 | 16.3 | 26.6 | 16.3 | 23.0 |
| $R_{SEI}$ [$\Omega$] | | 50.3 | | 110.5 | | 67.0 |
| $R_{ct}$ [$\Omega$] | 95.9 | 165.2 | 53.5 | 68.2 | 86.0 | 209.3 |

**Table 4.3.1:** ECM resistances from EIS fitting of the coin cell data before and after cycling.

Attempts were made to inspect what could have caused the low initial discharge capacity and rapid capacity fade of the coated cells. Therefore, a time dependent charge/discharge plot was created of the initial formation cycle at 0.1C, shown in Figure 4.3.3. As can be seen, both uncoated and coated cells consumed more charge than the practical capacity limit of NCA. Furthermore, the amount of excess charge consumption was higher for the coated cells compared to the pristine NCA cell, with a significant amount for 2505 NCA 3, which reached approximately 350 mAh g$^{-1}$.
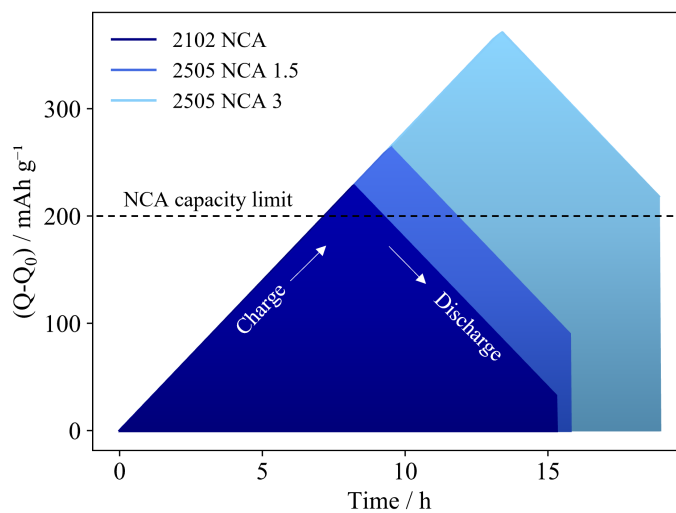
**Figure 4.3.3:** Initial charge and discharge at 0.1C for the pristine and coated NCA coin cells. The practical capacity limit of NCA is illustrated by the black dotted line. The tip of the triangles marks the transition from charging to discharging. The discharge ends where the downward slope breaks and goes vertical.

## 4.4 EIS of LPSC and LYC and Li-In alloy fabrication

### 4.4.1 Impedance spectroscopy study of LPSC and LYC

Figure 4.4.1 shows the extrapolated ionic conductivity of LYC and LPSC. It was extrapolated from the frequency independent plateaus at about the 10 - 100 kHz.
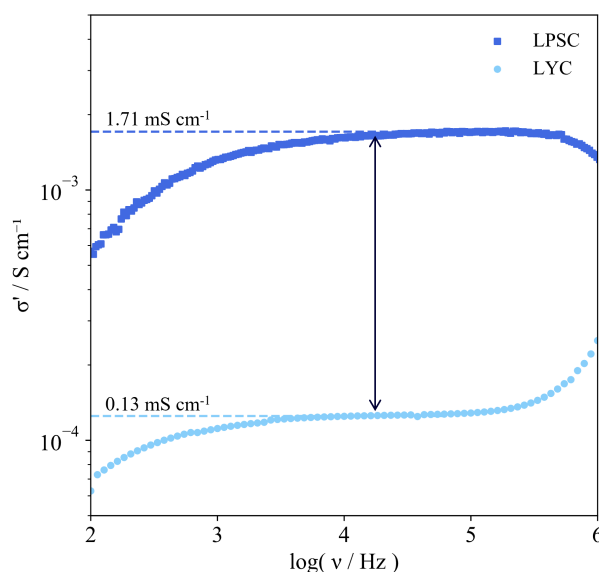


**Figure 4.4.1:** Conductivity plot of LYC and LPSC pellets under 250 MPa pressure.

The bulk resistance and conductivity of the two materials pressed at 250 MPa pressure are given in in Table 4.4.1. The ionic conductivity was extrapolated from the frequency independent plateaus in the Figure. The more than an order of magnitude higher ionic conductivity of LPSC compared to LYC, illustrates why minimising the LYC coating thickness is crucial for lowering internal resistance.

| Material | Bulk resistance / $\Omega$ | Pellet thickness / cm | Conductivity / $\mathrm{mS\,cm^{-1}}$ |
|----------|---------------------------|----------------------|----------------------------------------|
| LPSC     | 29                        | 0.039                | 1.71                                   |
| LYC      | 797                       | 0.079                | 0.13                                   |

**Table 4.4.1:** Bulk resistance and conductivity of the SEs utilised for the SSBs.

### 4.4.2 Lithiation of In foil

Figure 4.4.2 shows the lithiation of In-foil inside the coin cell setup described in Section 3.4.2 with a voltage versus time plot. A sharp decline in cell voltage can be seen

as lithium ions alloy into the In foil to form the Li-In phase. After approx. 1 minute, the cell has reached the stable cell voltage of 0.622 V. An IR drop of approximately 40 mV can be seen for the pulse discharges.
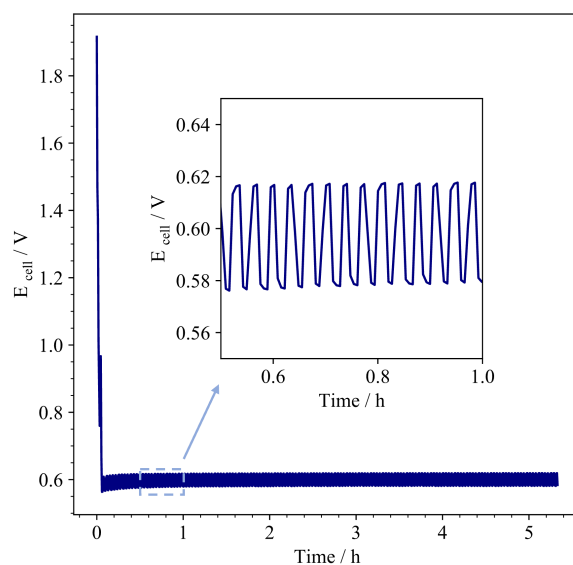


**Figure 4.4.2:** Time dependent voltage plot showing the successful lithiation of In foil to create the Li-In alloy used for the SSBs. The inset gives a clear view of the voltage drop and relaxation due to the pulse lithiation process.

## 4.5 Solid-state battery testing

In this section, similar to the conventional cells, GCPL measurements as well as EIS was performed in order to study the electrochemical performance of the SSBs. For better statistics, the average discharge capacity of three SSB cells were utilised for each of the pristine and coated cells. For the Coulombic efficiency plot, the average of two cells were used for the first eight cycles (not very informational, but it shows small deviations between the two samples) and three for the last twelve cycles. The standard deviation is included as error bars in the figures. Due to expected higher internal resistance than the conventional cells, the SSBs were charged and discharged at 0.1C to lower the IR drop. The voltage range utilised was 2.178 - 3.678 V (vs Li-In/Li$^+$). In Figure 4.5.1 and Figure 4.5.2, the SSBs were named a bit differently, to separate them from the coin cells. Cells utilising pristine NCA were named NCA while cells with 1.5 wt% LYC were named NCA 1.5 and cells with 3 wt% LYC were named NCA 3.

The different naming scheme proved beneficial, as the NCA SSBs showed poor initial
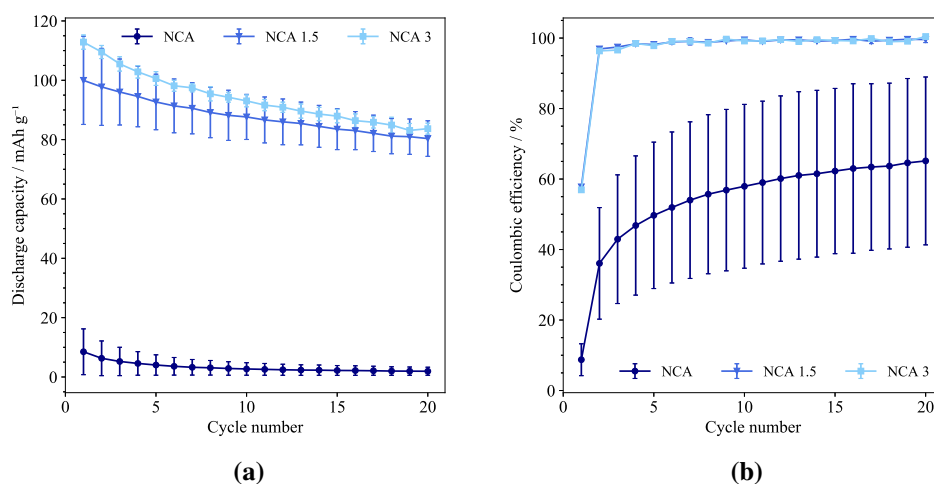


**Figure 4.5.1:** Cycling performance of SSB cells with pristine and coated NCA cathodes. NCA in navy, NCA 1.5 in royalblue and NCA 3 in lightskyblue. (a) Discharge capacity versus cycle number and (b) CE versus cycle number for the same battery cells.

discharge, unlike the 2102 NCA cells. In Figure 4.5.1(a), a significant difference in discharge capacity can be observed between the pristine and coated cells. The initial discharge capacity for NCA of 8.50 mAh g$^{-1}$ was less than 10% of the initial discharge capacity for NCA 1.5 and NCA 3 which were 100 mAh g$^{-1}$ and 113 mAh g$^{-1}$, respectively. In contrast to the coin cell cycling, the capacity fade was relatively slow. Between the coated SSBs it was slightly higher for the NCA 3 SSBs than the NCA

1.5 SSBs. After 20 cycles their discharge capacities were 83.7 $\mathrm{mAh\,g^{-1}}$ and 80.4 $\mathrm{mAh\,g^{-1}}$, respectively.

Although the capacity fade was slow for the SSBs, the ICE of 8.74% for NCA, 57.8% for NCA 1.5 and 56.9% for NCA 3 was low. However, the coated cells retain high average CE after the initial cycle, while the uncoated cell never comes close to 100% during the 20 cycles.

To gain further insights into the electrochemical performance and stability of the SSBs, EIS measurements were performed. Figure 4.5.2 shows the experimental data and fit after the 1st, 5th and 8th cycle of NCA 1.5 and NCA 3 SSBs, as well as EIS after 26 cycles for NCA and 20 cycles for NCA 1.5 and NCA 3. In the ECM utilised for fitting, bulk resistance, consisting of electrolyte grains and grain-boundaries, was modelled by $R_b$, while SEI/coating resistance and charge-transfer resistance was modelled by interface resistance $R_{int}$ in parallel with double-layer capacitance $CPE_{dl}$. It can be seen that the internal resistance of NCA 3 is lower than NCA 1.5 for each of the cycles shown. Furthermore, the interface resistance increases more for NCA 1.5 compared to NCA 3 from the 1st to the 8th cycle, while the bulk resistance of both SSBs remain stable. The quantitative values are provided in Table 4.5.1. It shows interface resistance increases from 67.4 $\Omega$ to 147.6 $\Omega$ for NCA 1.5 and from 38.4 $\Omega$ to 80.6 $\Omega$ for NCA 3.

| Cell | NCA 1.5 | | | NCA 3 | | |
|---|---|---|---|---|---|---|
| Cycle | 1st | 5th | 8th | 1st | 5th | 8th |
| $R_b/\Omega$ | 67.4 | 67.3 | 67.6 | 46.7 | 48.0 | 48.3 |
| $R_{int}/\Omega$ | 67.4 | 111.8 | 147.6 | 38.4 | 55.4 | 80.6 |

**Table 4.5.1:** Bulk and interface resistance for the SSBs NCA 1.5 and NCA 3 after the 1st, 5th and 8th cycle.

To provide context of the large deviation in cycling performance between the coated SSBs and the pristine one, EIS was performed of all cell types after cycling. To illustrate the results, Figure 4.5.2(d) shows the Nyquist plot of NCA after 26 cycles and NCA 1.5 and NCA 3 after 20 cycles. The interface resistance for the pristine NCA is about 50 and 100 times larger than for NCA 1.5 and NCA 3, respectively. Table 4.5.2 shows the significant difference quantitatively.
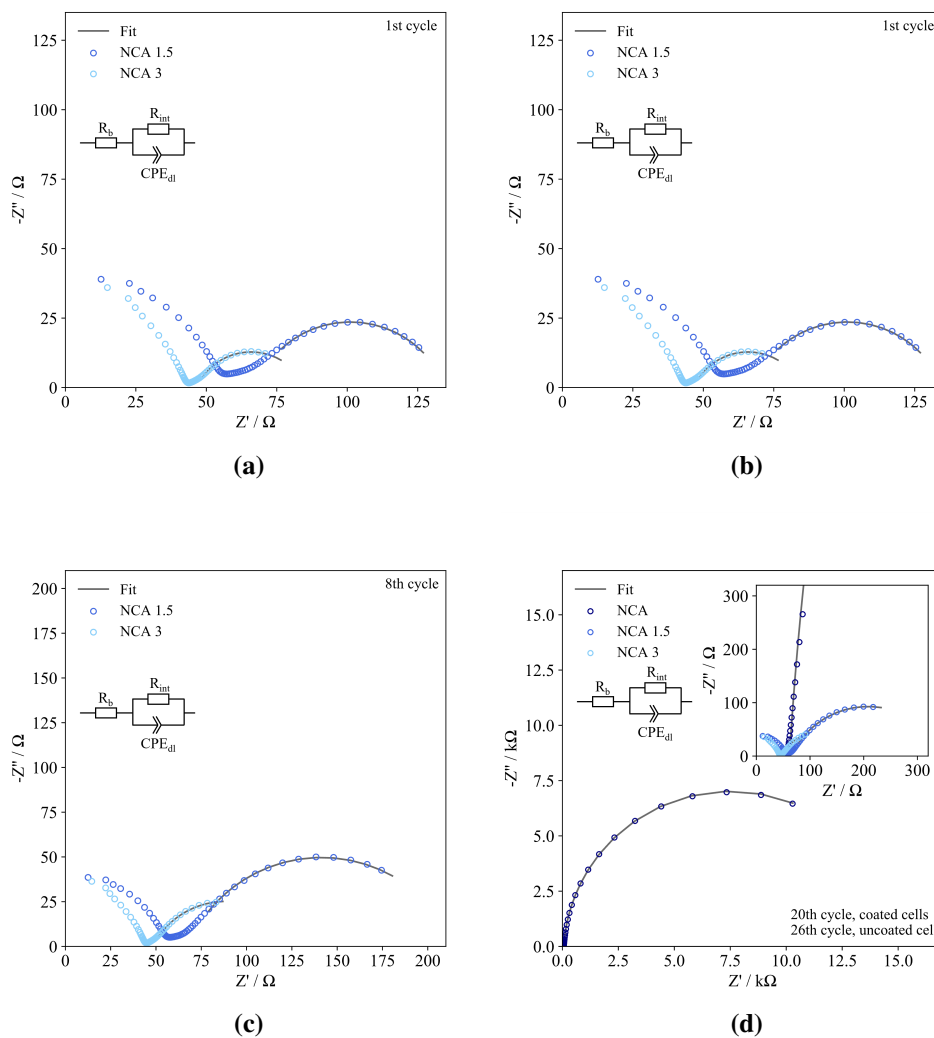
**Figure 4.5.2:** Nyquist plot of SSBs with ECM fits. EIS after the (a) 1$^{st}$, (b) 5$^{th}$ and (c) 8$^{th}$ cycle. (d) EIS of NCA 1.5 and NCA 3 after 20 cycles compared with NCA after 26 cycles. Inset to make semicircle of NCA 1.5 and NCA 3 visible.

| Cell | NCA | NCA 1.5 | NCA 3 |
|---|---|---|---|
| Cycle | 26$^{th}$ | 20$^{th}$ | 20$^{th}$ |
| $R_b/\Omega$ | 61.9 | 65.1 | 48.2 |
| $R_{int}/\Omega$ | 14906 | 286.1 | 144.2 |

**Table 4.5.2:** Bulk and interface resistance after 26 cycles for pristine NCA and 20 cycles for NCA 1.5 and NCA 3.

# Chapter 5

# Discussion

## 5.1 Dry-coating of NCA particles by mechanofusion

The difference in surface smoothness for the pristine and mechanofused NCA particles in Figure 4.2.1 and 4.2.2, respectively, is likely due to high compressive and shear forces during mechanofusion. During the process, the primary particles on the surface of the NCA secondary particles are deformed and sharp edges are smoothened, as described in Section 2.2.3. Zheng et al.[49] found that mechanofusion of NMC622 resulted in particle smoothing and that a 20 nm thin, amorphous surface layer was created during the process with the same composition as the core material. The deformation of the surface primary particles likely altered the crystallinity of these to result in this amorphous layer. The rounding effect of the secondary particles, observed in Figure 4.2.2(a), are likely caused by a similar smoothing mechanism as for the primary particles.

The STEM image in Figure 4.2.5 shows the porous and uneven 1.5 wt% LYC coating on an NCA secondary particle. One reason for the uneven coating could be due to the surface morphology of the pristine secondary particles. Nakamura et al.[29] found that during a dry coating process similar to mechanofusion, the coating particles initially created a discrete coating on the surface of the core particle. They found that after the initial discrete coating, upon further processing, the coating particles became deformed and started coalescing to result in a continuous coating layer. Due to the pronounced primary particles of pristine NCA, a significant amount of the LYC particles is consumed to cover the gaps between them. The likely result is an insufficient amount of coating material to create a continuous coating on the secondary particles.

Areas of thin or missing coating was therefore observed for the particles coated with 1.5 wt% LYC.

In contrast to Figure 4.2.5, a homogeneous thickness was observed for the 3 wt% LYC coated NCA particle, shown in Figure 4.2.6. With the pre-mechanofused NCA secondary particles, the surface had already been smoothened. The initial discrete coating of LYC particles would therefore result in a more even coating amount across the surface, due to fewer and narrower pits between primary particles. The following deformation and coalescence of LYC particles would produce a continuous coating with little variation in coating thickness.

## 5.2   Electrochemical performance of conventional cells

Several studies attribute the outperformance of LIBs utilising coated NCA cathodes mainly to two reasons. A continuous coating could mitigate or minimise side reactions between the cathode surface and the electrolyte[35]. It could also protect the cathode from HF attacks, where HF is generated from reactions between residual LiOH and $LiPF_6$ salt[51][7].

Similar to what has been reported by Qi et al.[35] and Chen et al.[7], the initial charge-transfer resistance of the coated cells was lower than for the 2102 NCA cell. However, after cycling, the resistance of 2505 NCA 3 was larger than for 2102 NCA, while it had only moderately increased for 2505 NCA 1.5. Pristine NCA has a tendency to develop cracks during cycling[16], which in turn exposes fresh electrolyte to the particle surface and causes SEI formation. Both 2102 NCA and 2505 NCA 3 likely experienced this. The 20 nanometer thin LYC coating is likely not able to withstand cracking from the volume contraction/expansion of NCA during cycling. The exposed areas cause electrolyte degradation and increase resistance. The thicker coating of the 1.5 wt% coated NCA cell should better withstand the volume contraction/expansion and possibly mitigate some of the cracking. Chen et al.[7] found that their pristine NCA cell and the cell with the least coating material had experienced cracking during cycling. Meanwhile, the thin LYC coating of 2505 NCA 3 would explain the relatively small SEI/coating resistance compared to the thick LYC coating for 2505 NCA 1.5 cell, as seen in Figure 4.3.2(b). The generally fast capacity fade of all cell types is likely also related to the large voltage range selected for the formation cycles. Pathan et al.[32] reported a positive correlation between larger voltage range and faster capacity fade.

Figure 4.3.3 showed that all the cell types consumed more than the practical capacity of NCA during the initial charge. This suggests that some competing side reactions are likely also taking place. The amount of additional charge consumed for the coated cells were higher than for the pristine NCA cell. The difference between pristine NCA and the 3 wt% coated NCA was significant. Furthermore, the disparity between charge consumed and delivered would indicate that the side reactions are likely irreversible. Some charge consumption due to the formation of an SEI at the interface between the electrolyte and the Li metal anode was to be expected, as described in Section 2.1.3. The anode side SEI will also crack, exposing fresh electrolyte and continuing to consume lithium and charge, due to the large volume expansion during cycling, but that can't explain the difference between the coated and uncoated NCA cells. They

both use Li metal anode, after all. However, some SEI formation is also expected at the cathode-electrolyte interface, with EC reacting chemically with reactive oxygen in the layered cathode oxide material at about 4.3 - 4.7 V (vs Li/Li$^+$), depending on the cathode material[19]. So those two SEI formations could probably explain the excess charge to side reactions of 2102 NCA.

In addition to SEI formation on the anode side, some reactions at the cathode side is expected for the coated cells. Calculations made by Wang et al.[44] showed that LYC had a thermodynamic oxidation limit of 4.21 V (vs Li/Li$^+$), which is below the 4.3 V upper cut-off limit selected for cycling. Due to the CV step and that the CV current stayed above the 0.05C limit of both the 2505 NCA 1.5 and 2505 NCA 3 cells, they remained at 4.3 V for about 2 hours (the set time limit). During that time, it is likely that the high current was due to continuous degradation of LYC, with the higher amount of LYC correlating with a larger excess charge consumption for 2505 NCA 3.

## 5.3 Electrochemical performance of solid-state cells

The low initial discharge capacity of the pristine NCA cells are likely due to severe side reactions at the interface between the LPSC electrolyte and the NCA electrode. Decomposition phases like $LiCl$, $Ni_3S_4$, $Li_3PO_4$ and oxygenated LPSC are likely, as Banerjee et al.[2] reported by XRD and Raman investigations for their similar NCA|LPSC|Li-In SSB. They also found that the decomposed species that are formed during the first charge mitigates subsequent electrochemical reactions between NCA and LPSC, due to the self-passivating nature of the interphases of LPSC and NCA. This can be seen from the cycles following for NCA, where the CE increases from cycle to cycle after the initial one. However, with such a low oxidation limit of about 2.2 V (vs Li/Li$^+$), the significant potential difference still favours oxidation reactions, which could explain why the CE stagnates at about 60%. Banerjee et al.[2] saw a large interface resistance of 1500 $\Omega$ and low CE of their NCA|LPSC|Li-In cell, which they attributed to parasitic side reactions at the electrode-electrolyte interface. The still low CE in Figure 4.5.1(b) after 20 cycles and almost 15000 $\Omega$ interface resistance after 26 cycles in Figure 4.5.2(d) for the NCA cell, indicates a continuous degradation and not only during the initial cycle. The rate of degradation slows down, however this can be explained by the low amount of charge stored during cycles and the passivating nature of the degradation products.

Unlike the coin cells, where more LYC in contact with the NCA seemed to be a detriment to cycling performance, Figure 4.5.1 indicated it was a benefit for the SSB cells. The SEM and STEM images in Figure 4.2.3(b) and Figure 4.2.5, respectively, showed some uncoated areas of the NCA surface which would lead to direct contact with LPSC. These areas would likely cause serious degradation of LPSC, compared to the lower degradation of LYC. The poor electronic conductivity of LYC should also contribute to lower discharge capacity, since electrons would need to be transported through the coating layer to travel between the NCA particles and conductive agents. Nakamura et al.[29] found a 94% decrease in electronic conductivity after coating NMC111 with another sulfide-based SE, $Li_3PS_4$. The resistance of ion transport through the LYC layer would also affect discharge capacity, but due to the intimate solid-solid contact between NCA and LYC, the contact resistance should be improved compared to the uncoated NCA cells. The generally higher interface resistance of NCA 1.5 versus NCA 3 in Figure 4.5.2 can likely be explained by larger resistance of ion transport through the thicker coating layer of NCA 1.5, as well as more severe electrolyte degradation at the uncoated surface areas. The difference in bulk resistance

is likely a result of the higher stack pressure for the particular NCA 3 cell of 70 MPa versus 61 MPa for the NCA 1.5 cell. The stack pressure could cause concerns regarding the cycling performance, however for sulfide-based SSBs, Doux et al. [11] found that it did not influence the cycling stability to any significant degree.

The LPSC/Li-In interface should also be discussed. An open circuit voltage of 0.622 volt (vs Li/Li$^+$) was achieved for all the Li-In alloys, meaning they were created successfully by following a similar lithiation procedure as Santhosha et al. [37]. They confirmed the interface stability of Li-In and $Li_3PS_4$, by utilising a symmetric cell setup of 1C cycling. An areal resistance of only 12 $\Omega\,cm^2$ was measured after 100 cycles. Furthermore, $LiNbO_3$-coated NMC811|$Li_{5.7}PS_{4.7}Cl_{1.3}$|Li-In SSB cells were cycled at 24 °C for 1000 cycles with a capacity retention above 90%, demonstrating highly stable Li-In-LPSC interface [47].

Although LYC coating facilitated SSB cycling to some degree, both NCA 1.5 and NCA 3 showed low ICE and unsatisfactory capacity fade during cycling. Removing the constant voltage step (as described in 3.3.4) of the cycling setup, reduced the time the applied charging potential was above the oxidation limit of LYC and the CE likely improved as a result.

The task of LYC as a coating material was mainly to improve interfacial stability at the cathode-electrolyte interface. For the conventional cells, LYC was less stable than the liquid electrolyte and failed to deliver on its task, ultimately resulting in poor electrochemical performance. However, for the SSB cells, LYC was substantially more stable than the sulfide-based SE and was able to improve the electrochemical performance.

# Chapter 6

# Conclusion

LYC-coated NCA cathodes were developed and integrated in SSBs, with the anticipation of enhanced electrochemical performance in regard to initial Coulombic efficiency and longer cycle life, compared to pristine NCA cathode. A scalable and solvent-free coating technique was adapted using mechofusion to develop thin coatings on the surface of NCA particles. Advanced characterisation tools such as FIB-SEM and STEM were utilized to investigate the developed samples. A successful dry-coating of LYC was revealed by the microscopy imaging and gave insights into the coating thickness and uniformity of the developed samples. The average coating thickness was 20 nm and uniformly covering the NCA particles. GCPL and EIS of pristine and LYC-coated NCA cathode SSBs showed a strong correlation between the reduced interface resistance of SSBs with LYC-coated NCA and their improved electrochemical performance, mainly due to mitigation of parasitic reactions at the cathode/electrolyte interface. However, electrochemical testing of LYC-coated NCA cathodes in cells with state-of-the-art liquid electrolyte demonstrated incompatibility between LYC and NCA, leading to poor discharge capacity and rapid capacity fade of the cells. The results demonstrated in this thesis showed that LYC coating could be utilized to improve electrochemical performance of SSBs with highly unstable SEs, e.g. LPSC. However, due to the limited electrochemical compatibility between LYC and high-voltage cathodes such as NCA, more suitable materials are desirable.

# Chapter 7

# Further Work

Given more time, a thorough post mortem analysis of the pristine and coated cells with FIB-SEM, TEM and XPS could give insights into which processes were taking place at the interface between the electrodes and SEs. To investigate how the NCA particle morphology and amount of coating material affects the coating process, more mechanofusion samples should be created and utilised for electrochemical testing. SSBs could also be cycled with an upper cut-off voltage of $4.2\,\mathrm{V}$ (vs Li/Li$^+$), which is below the theoretical thermodynamic oxidation limit of LYC. Any difference in electrochemical performance when switching to a lower voltage limit might give indications of the stability of LYC. Kobayashi et al.[22] recently demonstrated high capacity retention of LCO and LNMO cells utilising a $\beta - \mathrm{Li_3AlF_6}$ cathode coating. Developing variants of LYC to be utilised for coating, such as $\mathrm{Li_3YCl_{6-x}F_x}$, could potentially allow for materials with higher oxidation limits.

# Bibliography

[1] T. Asano et al. Solid Halide Electrolytes with High Lithium-Ion Conductivity for Application in 4 V Class Bulk-Type All-Solid-State Batteries. *Advanced Materials*, 30:1803075, 2018.

[2] A. Banerjee et al. Revealing Nanoscale Solid-Solid Interfacial Phenomena for Long-Life and High-Energy All-Solid-State Batteries. *ACS Applied Materials and Interfaces*, 11:43138–43145, 2019.

[3] Biologic. Protocols for studying intercalation electrodes materials-I: Galvanostatic cycling/potential limitations (GCPL) GITT – Battery AN 1. https://www.biologic.net/documents/gitt-electrochemistry-battery-application-note-1/, 2019.

[4] R. Bodine. Gas vs. Electric Car Fires [2022 Findings]. https://www.autoinsuranceez.com/gas-vs-electric-car-fires/, 2022. Accessed : 2022-06-13.

[5] Y.-W. Byeon and H. Kim. Review on Interface and Interphase Issues in Sulfide Solid-State Electrolytes for All-Solid-State Li-Metal Batteries. *Electrochem*, 2:452–471, 2021.

[6] C. Cao et al. A Sulfonimide-based Alternating Copolymer as a Single-ion Polymer Electrolyte for High-performance Lithium-ion Batteries. *Journal of Materials Chemistry A*, 5:22519–22526, 2017.

[7] J. Chen et al. Optimization of B2O3 coating process for NCA cathodes to achieve long-term stability for application in lithium ion batteries. *Energy*, 222:119913, 2021.

[8] Z. Chen, W. Zhang, and Z. Yang. A Review on Cathode Materials for Advanced Lithium Ion Batteries: Microstructure Designs and Performance Regulations. *Nanotechnology*, 31:012001, 2019.

June 26, 2022

[9] A. Cholewinski et al. Polymer Binders: Characterization and Development Toward Aqueous Electrode Fabrication for Sustainability. *Polymers*, 13:631, 2021.

[10] S. Cui et al. Optimized Temperature Effect of Li-Ion Diffusion with Layer Distance in $Li(Ni_xMn_yCo_z)O_2$ Cathode Materials for High Performance Li-Ion Battery. *Advanced Energy Materials*, 6:1501309, 2016.

[11] J. M. Doux et al. Pressure Effects on Sulfide Electrolytes for All Solid-state Batteries. *Journal of Materials Chemistry A*, 8:5049–5055, 2020.

[12] B. L. Ellis, K. T. Lee, and L. F. Nazar. Positive Electrode Materials for Li-Ion and Li-Batteries. *Chemistry of Materials*, 22:691, 2010.

[13] M. Foss. Powering Up: Global Battery Demand to Surge by 2030, Supply Headaches on the Horizon. https://www.rystadenergy.com/newsevents/news/press-releases/powering-up-global-battery-demand-to-surge-by-2030-supply-headaches-on-the-horizon/, 2022. Accessed : 2022-06-13.

[14] M. Golozar et al. Direct Observation of Lithium Metal Dendrites with Ceramic Solid Electrolyte. *Scientific Reports 2020 10:1*, 10:1–11, 2020.

[15] J. B. Goodenough and K.-S. Park. The Li-Ion Rechargeable Battery: A Perspective. *Journal of the American Chemical Society*, 135:1167–1176, 2013.

[16] Y. Han et al. Single- or Poly-Crystalline Ni-Rich Layered Cathode, Sulfide or Halide Solid Electrolyte: Which Will be the Winners for All-Solid-State Batteries? *Advanced Energy Materials*, 11:2100126, 2021.

[17] K. Ho Park et al. Design Strategies, Practical Considerations, and New Solution Processes of Sulfide Solid Electrolytes for All-Solid-State Batteries Solid-State Batteries. *Advanced Energy Materials*, 8:1800035, 2018.

[18] L. Hu, S. S. Zhang, and Z. Zhang. Electrolytes for Lithium and Lithium-ion Batteries. *Green Energy and Technology*, 172:231–261, 2015.

[19] R. Jung et al. Oxygen Release and Its Effect on the Cycling Stability of $LiNi_xMn_yCo_zO_2$ (NMC) Cathode Materials for Li-Ion Batteries. *Journal of The Electrochemical Society*, 164:A1361–A1377, 2017.

[20] Y. S. Jung et al. Issues and Challenges for Bulk-Type All-Solid-State Rechargeable Lithium Batteries Using Sulfide Solid Electrolytes. *Israel Journal of Chemistry*, 55:472–485, 2015.

[21] K. Kim et al. Material Design Strategy for Halide Solid Electrolytes $Li_3MX_6$ (X = Cl, Br, and I) for All-Solid-State High-Voltage Li-Ion Batteries. *Chemistry of Materials*, 33:3669–3677, 2021.

[22] H. Kobayashi et al. Effective $Li_3AlF_6$-Surface Coating for High-Voltage Lithium-Ion Battery Operation. *ACS Applied Energy Materials*, 4:9866–9870, 2021.

[23] T. Koç et al. In Search of the Best Solid Electrolyte-Layered Oxide Pairing for Assembling Practical All-Solid-State Batteries. *ACS Applied Energy Materials*, 4:13575–13585, 2021.

[24] L. Kong et al. Li-Ion Battery Fire Hazards and Safety Strategies. *Energies*, 11:2191, 2018.

[25] S. Luo et al. Growth of lithium-indium dendrites in all-solid-state lithium-based batteries with sulfide electrolytes. *Nature Communications*, 12:6968, 2021.

[26] Y. C. Lyu, J. Huang, and H. Li. Layered and Spinel Structural Cathodes. *Green Energy and Technology*, 172:67–92, 2015.

[27] N. Meddings et al. Application of Electrochemical Impedance Spectroscopy to Commercial Li-ion Cells: A Review. *Journal of Power Sources*, 480:228742, 2020.

[28] C. Monroe and J. Newman. The Impact of Elastic Deformation on Deposition Kinetics at Lithium/Polymer Interfaces. *Journal of The Electrochemical Society*, 152:A396, 2005.

[29] H. Nakamura et al. Dry Coating of Active Material Particles with Sulfide Solid Electrolytes for an All-Solid-state Lithium Battery. *Journal of Power Sources*, 448:227579, 2020.

[30] P. Nzereogu et al. Anode Materials for Lithium-ion Batteries: A Review. *Applied Surface Science Advances*, 9:100233, 2022.

[31] D. Ouyang et al. A Review on the Thermal Hazards of the Lithium-Ion Battery and the Corresponding Countermeasures. *Applied Sciences*, 9:2483, 2019.

[32] T. S. Pathan et al. Active Formation of Li-ion Batteries and its Effect on Cycle Life. *Journal of Physics: Energy*, 1:044003, 2019.

[33] R. Pfeffer et al. Synthesis of Engineered Particulates with Tailored Properties using Dry Particle Coating. *Powder Technology*, 117:40–67, 2001.

[34] F. Preishuber-Pflügl and M. Wilkening. Mechanochemically Synthesized Fluorides: Local Structures and Ion Transport. *Dalton Transactions*, 45:8675–8687, 2016.

[35] R. Qi et al. Improving the Stability of LiNi$_{0.80}$Co$_{0.15}$Al$_{0.05}$O$_2$ by AlPO$_4$ Nanocoating for Lithium-ion Batteries. *Science China Chemistry*, 60:1230–1235, 2017.

[36] Research Solutions & Resources LLC. Explaining the Constant Phase Element. http://consultrsr.net/resources/eis/cpe2.htm. Accessed: 2022-03-28.

[37] A. L. Santhosha et al. The IndiumLithium Electrode in Solid-State Lithium-Ion Batteries: Phase Formation, Redox Potentials, and Interface Stability. *Batteries Supercaps*, 2:524–529, 2019.

[38] R. Schlem et al. Mechanochemical Synthesis: A Tool to Tune Cation Site Disorder and Ionic Transport Properties of Li$_3$MCl$_6$ (M = Y, Er) Superionic Conductors. *Advanced Energy Materials*, 10:1903719, 2020.

[39] R. Schlem et al. Insights into the Lithium Sub-structure of Superionic Conductors. *Chemistry of Materials*, 33:337, 2021.

[40] R. Schlenker et al. Structure and Diffusion Pathways in Li$_6$PS$_5$Cl Argyrodite from Neutron Diffraction, Pair-Distribution Function Analysis, and NMR. *Chemistry of Materials*, 32:8420–8430, 2020.

[41] C. Tealdi, E. Quartarone, and P. Mustarelli. Solid-state Lithium Ion Electrolytes. *Green Energy and Technology*, 172:311–335, 2015.

[42] P. Vadhva et al. Electrochemical Impedance Spectroscopy for All-Solid-State Batteries: Theory, Methods and Future Outlook. *ChemElectroChem*, 8:1930–1947, 2021.

[43] Q. Wang et al. Confronting the Challenges in Lithium Anodes for Lithium Metal Batteries. *Advanced Science*, 8:2101111, 2021.

[44] S. Wang et al. Lithium Chlorides and Bromides as Promising Solid-State Chemistries for Fast Ion Conductors with Good Electrochemical Stability. *Angewandte Chemie International Edition*, 58:8039–8043, 2019.

[45] Z. Wu et al. Utmost Limits of Various Solid Electrolytes in All-Solid-state Lithium Batteries: A Critical Review. *Renewable and Sustainable Energy Reviews*, 109:367–385, 2019.

[46] K. Zaghib, A. Mauger, and C. M. Julien. Olivine-based Cathode Materials. *Green Energy and Technology*, 172:25–65, 2015.

[47] D. Zeng et al. Promoting favorable interfacial properties in lithium-based batteries using chlorine-rich sulfide inorganic solid-state electrolytes. *Nature Communications*, 13:1–13, 2022.

[48] S. S. Zhang, K. Xu, and T. R. Jow. Study of the Charging Process of a $LiCoO_2$-based Li-ion Battery. *Journal of Power Sources*, 160:1349–1354, 2006.

[49] L. Zheng et al. Spherically Smooth Cathode Particles by Mechanofusion Processing. *Journal of The Electrochemical Society*, 166:A2924–A2927, 2019.

[50] L. Zheng, T. D. Hatchard, and M. N. Obrovac. A High-quality Mechanofusion Coating for Enhancing Lithium-ion Battery Cathode Material Performance. *MRS Communications*, 9:245–250, 2019.

[51] P. Zhou et al. $SiO_2$-coated $LiNi_{0.915}Co_{0.075}Al_{0.01}O_2$ Cathode Material for Rechargeable Li-ion Batteries. *Nanoscale*, 8:19263–19269, 2016.

[52] Y. Zhu, X. He, and Y. Mo. Origin of Outstanding Stability in the Lithium Solid Electrolyte Materials: Insights from Thermodynamic Analyses Based on First-Principles Calculations. *ACS Applied Materials and Interfaces*, 7:23685–23693, 2015.

[53] Y. Zhu, X. He, and Y. Mo. First Principles Study on Electrochemical and Chemical Stability of Solid Electrolyte-Electrode Interfaces in All-Solid-state Li-ion Batteries. *Journal of Materials Chemistry A*, 4:3253–3266, 2016.

# Appendix A

# Python code

This is the Python code utilised for plotting the different figures in the thesis.

```python
import pandas as pd
import numpy as np
import matplotlib.pyplot as plt

plt.rcParams.update({'font.size': 15})
plt.rcParams.update({'font.family': 'serif'})
plt.rcParams.update({'font.serif': 'Times New Roman'})
plt.rcParams.update({'mathtext.default':  'regular' })

def GCPLToCycleCapacity(file):
    'file: mtp/txt'
    'Takes in a file, returns cycle data and specific capacity
    for each cycle'
    df = pd.read_csv(file, sep = r'\t', skiprows=1)
    cycle_array = df.iloc[:, [0]].to_numpy()
    cap_array = df.iloc[:, [1]].to_numpy()
    return cycle_array, cap_array

def CycleVsCapAndEff(file):
    'file: mtp/txt'
    'Takes in a file, returns cycle data, specific capacity and
    coulombic efficiency for each cycle'
    df = pd.read_csv(file, sep=r'\t', skiprows=0)
    cycle_array = df.iloc[:, [0]].to_numpy()
    cap_array = df.iloc[:, [2]].to_numpy()
    eff_array = df.iloc[:, [3]].to_numpy()
    return cycle_array, cap_array, eff_array
```

```
26
27  def GCPLToEfficiency(file):
28      'file: mtp/txt'
29      'Takes in a file, returns Coulombic efficiency for each cycle
        '
30      df = pd.read_csv(file, sep=r'\t', skiprows=1)
31      eff_array = df.iloc[:, [1]].to_numpy()
32      return eff_array
33
34  def PEISToNyquist(file):
35      'Takes in a .txt file and returns an array of Real Z and
        Imaginary Z'
36      data = pd.read_csv(file, sep = r'\t', skiprows = 1)
37      real_Z = data.loc[:, ['Re(Z)/Ohm']]
38      im_Z = data.loc[:, ['-Im(Z)/Ohm']]
39      real_array = real_Z.to_numpy()
40      im_array = im_Z.to_numpy()
41      return real_array, im_array
42
43  def AvgAndStdDevOfCapacities(cap1, cap2, cap3):
44      'Takes in the capacity of 3 cells and returns the average and
        std deviation.'
45      length = len(cap1)
46      if len(cap2) < length:
47          length = len(cap2)
48      if len(cap3) < length:
49          length = len(cap3)
50      three_col_caps = np.concatenate([cap1[:length], cap2[:length
    ], cap3[:length]], axis = 1)
51      avg_cap = []
52      std_dev = []
53      for i in range(len(three_col_caps)):
54          avg_cap.append(np.mean(three_col_caps[i]))
55          std_dev.append(np.std(three_col_caps[i]))
56      return avg_cap, std_dev
57
58  def AvgAndStdDev2DataSets(cap1, cap2):
59      'Takes in the capacity of 2 cells and returns average and std
        deviation.'
60      length = len(cap1)
61      if len(cap2) < length:
62          length = len(cap2)
63      two_col_caps = np.concatenate([cap1[:length], cap2[:length]],
        axis = 1)
```

```
64      avg_cap = []
65      std_dev = []
66      for i in range(len(two_col_caps)):
67          avg_cap.append(np.mean(two_col_caps[i]))
68          std_dev.append(np.std(two_col_caps[i]))
69      return avg_cap, std_dev
70
71  def Avg2PlusAvg3(avg2, avg3):
72      'Just some for a bit of time saving'
73      return np.concatenate([avg2, avg3])
74
75
76  'Li-In plating'
77  li_in = pd.read_csv(r"C:\Users\toggy\Desktop\OneDrive\
        Masteroppgave\Li-In\Cell10_time_vs_Ecell.txt", sep = '\t',
        skiprows=1)
78  li_in_time = li_in.iloc[:, [0]].to_numpy()/3600
79  li_in_Ecell = li_in.iloc[:, [1]].to_numpy()
80  fig, ax1 = plt.subplots(figsize = (6,6))
81  ax1.plot(li_in_time, li_in_Ecell, 'navy')
82  left, bottom, width, height = [0.35, 0.35, 0.4, 0.4]
83  ax2 = fig.add_axes([left, bottom, width, height])
84  ax2.set_xlim(0.5, 1.0)
85  ax2.set_ylim(0.55, 0.65)
86  ax2.set_xlabel('Time / h')
87  ax2.set_ylabel('E $_{cell}$ / V')
88  ax2.plot(li_in_time, li_in_Ecell, 'navy')
89  ax1.set_xticks([0,1,2,3,4,5])
90  ax1.minorticks_on()
91  ax1.set_xlabel('Time / h')
92  ax1.set_ylabel('E $_{cell}$ / V')
93  plt.show()
94
95  'Charge/discharge initial cycling C/10 coin cells'
96  NCA_2C_time_sec, NCA_2C_charge = GCPLToCycleCapacity(r"C:\Users\
        toggy\Desktop\OneDrive\Masteroppgave\Cycle data\Torgeir\
        Charge_v_time\2102_2C_charge_1st_cyc.txt")
97  NCA_2C_time_sec_from_0 = NCA_2C_time_sec-NCA_2C_time_sec[0]
98  NCA_2C_time_hour = NCA_2C_time_sec_from_0/3600
99  NCA_15wt_time_sec, NCA_15wt_charge = GCPLToCycleCapacity(r"C:\
        Users\toggy\Desktop\OneDrive\Masteroppgave\Cycle data\Torgeir
        \Charge_v_time\2505_1.5wt_1_1st_cyc.txt")
100 NCA_15wt_time_sec_from_0 = NCA_15wt_time_sec-NCA_15wt_time_sec[0]
101 NCA_15wt_time_hour = NCA_15wt_time_sec_from_0/3600
```

```
102 NCA_3wt_time_sec , NCA_3wt_charge = GCPLToCycleCapacity(r"C:\Users
       \toggy\Desktop\OneDrive\Masteroppgave\Cycle data\Torgeir\
       Charge_v_time\2505_3wt_2_1st_cyc.txt")
103 NCA_3wt_time_sec_from_0 = NCA_3wt_time_sec-NCA_3wt_time_sec[0]
104 NCA_3wt_time_hour = NCA_3wt_time_sec_from_0/3600
105 plt.plot(NCA_2C_time_hour , NCA_2C_charge , color = 'navy', label =
        '2102 NCA', zorder = 1)
106 plt.plot(NCA_15wt_time_hour , NCA_15wt_charge , color = 'royalblue'
       , label = '2505 NCA 1.5', zorder = -2)
107 plt.plot(NCA_3wt_time_hour , NCA_3wt_charge , color = 'lightskyblue
       ', label = '2505 NCA 3', zorder = -3)
108 plt.legend(loc = 'upper left', fontsize = 13, ncol = 1, frameon =
        False)
109 plt.xlabel('Time / h')
110 plt.ylabel('(Q-Q$_{0}$) / mAh g\u207B\u00B9')
111 plt.show()
112
113 'Plotting SSB cells. Specific capacity and Coulombic efficiency
       vs cycle number.'
114 HC2_cyc , HC2_cap , HC2_eff = CycleVsCapAndEff(r"C:\Users\toggy\
       Desktop\OneDrive\Masteroppgave\6mg_load_HC2_009_3.txt")
        #'NCA'
115 HC3_cyc , HC3_cap , HC3_eff = CycleVsCapAndEff(r"C:\Users\toggy\
       Desktop\OneDrive\Masteroppgave\6mg_load_HC3_009_1~2.txt")
              #'NCA3'
116 HC4_cyc , HC4_cap , HC4_eff = CycleVsCapAndEff(r"C:\Users\toggy\
       Desktop\OneDrive\Masteroppgave\6mg_load_HC4_009_8.txt")
        #'NCA'
117 HC5_cyc , HC5_cap , HC5_eff = CycleVsCapAndEff(r"C:\Users\toggy\
       Desktop\OneDrive\Masteroppgave\6mg_load_HC5_009_6.txt")
        #'NCA'
118 HC7_cyc , HC7_cap , HC7_eff = CycleVsCapAndEff(r"C:\Users\toggy\
       Desktop\OneDrive\Masteroppgave\6mg_load_HC7_009_6.txt")
        #'NCA1.5'
119 HC9_cyc , HC9_cap , HC9_eff = CycleVsCapAndEff(r"C:\Users\toggy\
       Desktop\OneDrive\Masteroppgave\6mg_load_HC9_009_8.txt")
        #'NCA3'
120 HC10_cyc , HC10_cap , HC10_eff = CycleVsCapAndEff(r"C:\Users\toggy\
       Desktop\OneDrive\Masteroppgave\6mg_load_HC10_009_7.txt")   #'
       NCA1.5'
121 HC6_cyc , HC6_cap = GCPLToCycleCapacity(r"C:\Users\toggy\Desktop\
       OneDrive\Masteroppgave\NCA_Li-In_HC\6_mg_load_HC_6\cyc_vs_cap
       \HC_6.txt")    #NCA1.5
```

```
122 HC6_eff = GCPLToEfficiency(r"C:\Users\toggy\Desktop\OneDrive\
        Masteroppgave\NCA_Li-In_HC\6_mg_load_HC_6\cyc_v_eff\HC_6.txt"
        )
123 HC8_cyc, HC8_cap = GCPLToCycleCapacity(r"C:\Users\toggy\Desktop\
        OneDrive\Masteroppgave\NCA_Li-In_HC\6_mg_load_HC_8\cyc_v_cap\
        HC_8.txt")      #NCA3
124 HC8_eff = GCPLToEfficiency(r"C:\Users\toggy\Desktop\OneDrive\
        Masteroppgave\NCA_Li-In_HC\6_mg_load_HC_8\cyc_v_eff\HC_8.txt"
        )
125
126 NCA_avg_cap, NCA_std_dev = AvgAndStdDevOfCapacities(HC2_cap,
        HC4_cap, HC5_cap)
127 NCA_avg_eff, NCA_eff_dev = AvgAndStdDevOfCapacities(HC2_eff,
        HC4_eff, HC5_eff)
128 NCA3_avg_cap, NCA3_std_dev = AvgAndStdDevOfCapacities(HC3_cap,
        HC8_cap, HC9_cap)
129 # NCA3_avg_eff, NCA3_eff_dev = AvgAndStdDevOfCapacities(HC3_eff,
        HC8_eff, HC9_eff)
130 NCA3_1st_avg_eff, NCA3_1st_dev_eff = AvgAndStdDev2DataSets(
        HC3_eff[:9], HC9_eff[:9])
131 NCA3_last_avg_eff, NCA3_last_dev_eff = AvgAndStdDevOfCapacities(
        HC3_eff[9:20], HC8_eff, HC9_eff[9:20])
132 NCA3_avg_eff, NCA3_eff_dev = Avg2PlusAvg3(NCA3_1st_avg_eff,
        NCA3_last_avg_eff), Avg2PlusAvg3(NCA3_1st_dev_eff,
        NCA3_last_dev_eff)
133 NCA15_avg_cap, NCA15_std_dev = AvgAndStdDevOfCapacities(HC6_cap,
        HC7_cap, HC10_cap)
134 # NCA15_avg_eff, NCA15_eff_dev = AvgAndStdDevOfCapacities(HC6_eff
        , HC7_eff, HC10_eff)
135 NCA15_1st_avg_eff, NCA15_1st_dev_eff = AvgAndStdDev2DataSets(
        HC7_eff[:9], HC10_eff[:9])
136 NCA15_last_avg_eff, NCA15_last_dev_eff = AvgAndStdDevOfCapacities
        (HC7_eff[9:20], HC6_eff, HC10_eff[9:20])
137 NCA15_avg_eff, NCA15_eff_dev = Avg2PlusAvg3(NCA15_1st_avg_eff,
        NCA15_last_avg_eff), Avg2PlusAvg3(NCA15_1st_dev_eff,
        NCA15_last_dev_eff)
138 print(NCA_avg_eff[0])
139 print(NCA15_avg_eff[0])
140 print(NCA3_avg_eff[0])
141 cycles = [x+1 for x in range(20)]
142 fig, ax1 = plt.subplots(figsize = (6,6))
143 ax1.errorbar(cycles, NCA_avg_cap[:20], yerr = NCA_std_dev[:20],
        ecolor = 'navy', color = 'navy', capsize = 2, marker = 'o',
        ms = 5, label = 'NCA')
```

```
144  ax1.errorbar(cycles, NCA15_avg_cap[:20], yerr = NCA15_std_dev
         [:20], ecolor = 'royalblue', color = 'royalblue', capsize =
         2, marker = 'v', ms = 5, label = 'NCA 1.5')
145  ax1.errorbar(cycles, NCA3_avg_cap[:20], yerr = NCA3_std_dev[:20],
          ecolor = 'lightskyblue', color = 'lightskyblue', capsize =
         2, marker = 's', ms = 5, label = 'NCA 3')
146  # ax1.errorbar(cycles, NCA_avg_eff[:20], yerr = NCA_eff_dev[:20],
          ecolor = 'navy', color = 'navy', capsize = 2, marker = 'o',
         ms = 5, label = 'NCA')
147  # ax1.errorbar(cycles, NCA15_avg_eff, yerr = NCA15_eff_dev,
         ecolor = 'royalblue', color = 'royalblue', capsize = 2,
         marker = 'v', ms = 5, label = 'NCA 1.5')
148  # ax1.errorbar(cycles, NCA3_avg_eff, yerr = NCA3_eff_dev, ecolor
         = 'lightskyblue', color = 'lightskyblue', capsize = 2, marker
          = 's', ms = 5, label = 'NCA 3')
149  # ax1.set_ylim(0, 150)
150  ax1.set_ylabel('Discharge capacity / mAh g\u207B\u00B9')
151  ax1.set_xlabel('Cycle number')
152  # ax1.set_ylabel('Coulombic efficiency / %')
153  ax1.minorticks_on()
154  ax1.set_xticks([0, 5, 10, 15, 20])
155  ax1.xaxis.set_tick_params(which='minor', bottom=False)
156  ax1.legend(loc = 'upper right', ncol = 3, fontsize = 13, frameon
         = False)
157  plt.show()
158
159  'SSB EIS coated cells 1st-8th cycle'
160  HC6_15wt_re_03, HC6_15wt_im_03 = PEISToNyquist(r"C:\Users\toggy\
         Desktop\OneDrive\Masteroppgave\NCA_Li-In_HC\6_mg_load_HC_6\
         EIS_exp_data\03.txt")
161  HC6_15wt_re_05, HC6_15wt_im_05 = PEISToNyquist(r"C:\Users\toggy\
         Desktop\OneDrive\Masteroppgave\NCA_Li-In_HC\6_mg_load_HC_6\
         EIS_exp_data\05.txt")
162  HC6_15wt_re_07, HC6_15wt_im_07 = PEISToNyquist(r"C:\Users\toggy\
         Desktop\OneDrive\Masteroppgave\NCA_Li-In_HC\6_mg_load_HC_6\
         EIS_exp_data\07.txt")
163  HC6_15wt_re_09, HC6_15wt_im_09 = PEISToNyquist(r"C:\Users\toggy\
         Desktop\OneDrive\Masteroppgave\NCA_Li-In_HC\6_mg_load_HC_6\
         EIS_exp_data\09.txt")
164  HC6_15wt_re_11, HC6_15wt_im_11 = PEISToNyquist(r"C:\Users\toggy\
         Desktop\OneDrive\Masteroppgave\NCA_Li-In_HC\6_mg_load_HC_6\
         EIS_exp_data\11.txt")
165  HC6_15wt_re_13, HC6_15wt_im_13 = PEISToNyquist(r"C:\Users\toggy\
         Desktop\OneDrive\Masteroppgave\NCA_Li-In_HC\6_mg_load_HC_6\
```

```
      EIS_exp_data\13.txt")
166 HC6_15wt_re_15 , HC6_15wt_im_15 = PEISToNyquist(r"C:\Users\toggy\
      Desktop\OneDrive\Masteroppgave\NCA_Li-In_HC\6_mg_load_HC_6\
      EIS_exp_data\15.txt")
167 HC6_15wt_re_17 , HC6_15wt_im_17 = PEISToNyquist(r"C:\Users\toggy\
      Desktop\OneDrive\Masteroppgave\NCA_Li-In_HC\6_mg_load_HC_6\
      EIS_exp_data\17.txt")
168 HC6_15wt_fit_re_03 , HC6_15wt_fit_im_03 = PEISToNyquist(r"C:\Users
      \toggy\Desktop\OneDrive\Masteroppgave\NCA_Li-In_HC\6
      _mg_load_HC_6\EIS_fits\Zfit_plots\HC6_03.txt")
169 HC6_15wt_fit_re_05 , HC6_15wt_fit_im_05 = PEISToNyquist(r"C:\Users
      \toggy\Desktop\OneDrive\Masteroppgave\NCA_Li-In_HC\6
      _mg_load_HC_6\EIS_fits\Zfit_plots\HC6_05.txt")
170 HC6_15wt_fit_re_07 , HC6_15wt_fit_im_07 = PEISToNyquist(r"C:\Users
      \toggy\Desktop\OneDrive\Masteroppgave\NCA_Li-In_HC\6
      _mg_load_HC_6\EIS_fits\Zfit_plots\HC6_07.txt")
171 HC6_15wt_fit_re_09 , HC6_15wt_fit_im_09 = PEISToNyquist(r"C:\Users
      \toggy\Desktop\OneDrive\Masteroppgave\NCA_Li-In_HC\6
      _mg_load_HC_6\EIS_fits\Zfit_plots\HC6_09.txt")
172 HC6_15wt_fit_re_11 , HC6_15wt_fit_im_11 = PEISToNyquist(r"C:\Users
      \toggy\Desktop\OneDrive\Masteroppgave\NCA_Li-In_HC\6
      _mg_load_HC_6\EIS_fits\Zfit_plots\HC6_11.txt")
173 HC6_15wt_fit_re_13 , HC6_15wt_fit_im_13 = PEISToNyquist(r"C:\Users
      \toggy\Desktop\OneDrive\Masteroppgave\NCA_Li-In_HC\6
      _mg_load_HC_6\EIS_fits\Zfit_plots\HC6_13.txt")
174 HC6_15wt_fit_re_15 , HC6_15wt_fit_im_15 = PEISToNyquist(r"C:\Users
      \toggy\Desktop\OneDrive\Masteroppgave\NCA_Li-In_HC\6
      _mg_load_HC_6\EIS_fits\Zfit_plots\HC6_15.txt")
175 HC6_15wt_fit_re_17 , HC6_15wt_fit_im_17 = PEISToNyquist(r"C:\Users
      \toggy\Desktop\OneDrive\Masteroppgave\NCA_Li-In_HC\6
      _mg_load_HC_6\EIS_fits\Zfit_plots\HC6_17.txt")
176
177
178 HC8_3wt_re_03 , HC8_3wt_im_03 = PEISToNyquist(r"C:\Users\toggy\
      Desktop\OneDrive\Masteroppgave\NCA_Li-In_HC\6_mg_load_HC_8\
      EIS_exp_data\03.txt")
179 HC8_3wt_re_05 , HC8_3wt_im_05 = PEISToNyquist(r"C:\Users\toggy\
      Desktop\OneDrive\Masteroppgave\NCA_Li-In_HC\6_mg_load_HC_8\
      EIS_exp_data\05.txt")
180 HC8_3wt_re_07 , HC8_3wt_im_07 = PEISToNyquist(r"C:\Users\toggy\
      Desktop\OneDrive\Masteroppgave\NCA_Li-In_HC\6_mg_load_HC_8\
      EIS_exp_data\07.txt")
181 HC8_3wt_re_09 , HC8_3wt_im_09 = PEISToNyquist(r"C:\Users\toggy\
      Desktop\OneDrive\Masteroppgave\NCA_Li-In_HC\6_mg_load_HC_8\
```

```
      EIS_exp_data\09.txt")
182 HC8_3wt_re_11, HC8_3wt_im_11 = PEISToNyquist(r"C:\Users\toggy\
      Desktop\OneDrive\Masteroppgave\NCA_Li-In_HC\6_mg_load_HC_8\
      EIS_exp_data\11.txt")
183 HC8_3wt_re_13, HC8_3wt_im_13 = PEISToNyquist(r"C:\Users\toggy\
      Desktop\OneDrive\Masteroppgave\NCA_Li-In_HC\6_mg_load_HC_8\
      EIS_exp_data\13.txt")
184 HC8_3wt_re_15, HC8_3wt_im_15 = PEISToNyquist(r"C:\Users\toggy\
      Desktop\OneDrive\Masteroppgave\NCA_Li-In_HC\6_mg_load_HC_8\
      EIS_exp_data\15.txt")
185 HC8_3wt_re_17, HC8_3wt_im_17 = PEISToNyquist(r"C:\Users\toggy\
      Desktop\OneDrive\Masteroppgave\NCA_Li-In_HC\6_mg_load_HC_8\
      EIS_exp_data\17.txt")
186 HC8_3wt_fit_re_03, HC8_3wt_fit_im_03 = PEISToNyquist(r"C:\Users\
      toggy\Desktop\OneDrive\Masteroppgave\NCA_Li-In_HC\6
      _mg_load_HC_8\EIS_fits\Zfit_plots\HC8_03.txt")
187 HC8_3wt_fit_re_05, HC8_3wt_fit_im_05 = PEISToNyquist(r"C:\Users\
      toggy\Desktop\OneDrive\Masteroppgave\NCA_Li-In_HC\6
      _mg_load_HC_8\EIS_fits\Zfit_plots\HC8_05.txt")
188 HC8_3wt_fit_re_07, HC8_3wt_fit_im_07 = PEISToNyquist(r"C:\Users\
      toggy\Desktop\OneDrive\Masteroppgave\NCA_Li-In_HC\6
      _mg_load_HC_8\EIS_fits\Zfit_plots\HC8_07.txt")
189 HC8_3wt_fit_re_09, HC8_3wt_fit_im_09 = PEISToNyquist(r"C:\Users\
      toggy\Desktop\OneDrive\Masteroppgave\NCA_Li-In_HC\6
      _mg_load_HC_8\EIS_fits\Zfit_plots\HC8_09.txt")
190 HC8_3wt_fit_re_11, HC8_3wt_fit_im_11 = PEISToNyquist(r"C:\Users\
      toggy\Desktop\OneDrive\Masteroppgave\NCA_Li-In_HC\6
      _mg_load_HC_8\EIS_fits\Zfit_plots\HC8_11.txt")
191 HC8_3wt_fit_re_13, HC8_3wt_fit_im_13 = PEISToNyquist(r"C:\Users\
      toggy\Desktop\OneDrive\Masteroppgave\NCA_Li-In_HC\6
      _mg_load_HC_8\EIS_fits\Zfit_plots\HC8_13.txt")
192 HC8_3wt_fit_re_15, HC8_3wt_fit_im_15 = PEISToNyquist(r"C:\Users\
      toggy\Desktop\OneDrive\Masteroppgave\NCA_Li-In_HC\6
      _mg_load_HC_8\EIS_fits\Zfit_plots\HC8_15.txt")
193 HC8_3wt_fit_re_17, HC8_3wt_fit_im_17 = PEISToNyquist(r"C:\Users\
      toggy\Desktop\OneDrive\Masteroppgave\NCA_Li-In_HC\6
      _mg_load_HC_8\EIS_fits\Zfit_plots\HC8_17.txt")
194
195 fig, ax1 = plt.subplots(figsize = (6,6)) #1st cycle
196 ax1.scatter(HC6_15wt_re_03[:55], HC6_15wt_im_03[:55], marker='o',
       s = 25, facecolors = 'none', edgecolors = 'royalblue', label
       = 'NCA 1.5')
197 ax1.plot(HC6_15wt_fit_re_03, HC6_15wt_fit_im_03, color = 'dimgray
      ', zorder = -1, label = 'Fit')
```

```
198 ax1.scatter(HC8_3wt_re_03[:55], HC8_3wt_im_03[:55], marker='o', s
       = 25, facecolors = 'none', edgecolors = 'lightskyblue',
       label = 'NCA 3')
199 ax1.plot(HC8_3wt_fit_re_03, HC8_3wt_fit_im_03, color = 'dimgray',
       zorder = -1)
200 ax1.set_xlabel('Z\' / \u2126')
201 ax1.set_ylabel('-Z\'\' / \u2126')
202 ax1.legend(loc = 'upper left', fontsize = 13, ncol = 1, frameon =
       False)
203 ax1.set_ylim(0, 135)
204 ax1.set_xlim(0, 135)
205 ax1.set_xticks([0, 25, 50, 75, 100, 125])
206 ax1.set_yticks([0, 25, 50, 75, 100, 125])
207 ax1.text(0.84, 0.98, '1st cycle', transform=ax1.transAxes,
       fontsize=13, verticalalignment='top')
208 plt.show()
209
210 fig, ax1 = plt.subplots(figsize = (6,6)) #5th cycle
211 ax1.scatter(HC6_15wt_re_11[:55], HC6_15wt_im_11[:55], marker='o',
       s = 25, facecolors = 'none', edgecolors = 'royalblue', label
       = 'NCA 1.5')
212 ax1.plot(HC6_15wt_fit_re_11, HC6_15wt_fit_im_11, color = 'dimgray
       ', zorder = -1, label = 'Fit')
213 ax1.scatter(HC8_3wt_re_11[:55], HC8_3wt_im_11[:55], marker='o', s
       = 25, facecolors = 'none', edgecolors = 'lightskyblue',
       label = 'NCA 3')
214 ax1.plot(HC8_3wt_fit_re_11, HC8_3wt_fit_im_11, color = 'dimgray',
       zorder = -1)
215 ax1.set_xlabel('Z\' / \u2126')
216 ax1.set_ylabel('-Z\'\' / \u2126')
217 ax1.legend(loc = 'upper left', fontsize = 13, ncol = 1, frameon =
       False)
218 ax1.set_ylim(0, 185)
219 ax1.set_xlim(0, 185)
220 ax1.set_xticks([0, 25, 50, 75, 100, 125, 150, 175])
221 ax1.set_yticks([0, 25, 50, 75, 100, 125, 150, 175])
222 ax1.text(0.84, 0.98, '5th cycle', transform=ax1.transAxes,
       fontsize=13, verticalalignment='top')
223 plt.show()
224
225 fig, ax1 = plt.subplots(figsize = (6,6)) #8th cycle
226 ax1.scatter(HC6_15wt_re_17[:55], HC6_15wt_im_17[:55], marker='o',
       s = 25, facecolors = 'none', edgecolors = 'royalblue', label
       = 'NCA 1.5')
```

```
227 ax1.plot(HC6_15wt_fit_re_17, HC6_15wt_fit_im_17, color = 'dimgray
        ', zorder = -1, label = 'Fit')
228 ax1.scatter(HC8_3wt_re_17[:55], HC8_3wt_im_17[:55], marker='o', s
        = 25, facecolors = 'none', edgecolors = 'lightskyblue',
        label = 'NCA 3')
229 ax1.plot(HC8_3wt_fit_re_17, HC8_3wt_fit_im_17, color = 'dimgray',
         zorder = -1)
230 ax1.set_xlabel('Z\' / \u2126')
231 ax1.set_ylabel('-Z\'\' / \u2126')
232 ax1.legend(loc = 'upper left', fontsize = 13, ncol = 1, frameon =
         False)
233 ax1.set_ylim(0, 210)
234 ax1.set_xlim(0, 210)
235 ax1.set_xticks([0, 25, 50, 75, 100, 125, 150, 175, 200])
236 ax1.set_yticks([0, 25, 50, 75, 100, 125, 150, 175, 200])
237 ax1.text(0.84, 0.98, '8th cycle', transform=ax1.transAxes,
        fontsize=13, verticalalignment='top')
238 plt.show()
239
240 'SSB EIS coated and uncoated cycle 20 coated vs 26 uncoated'
241 HC4_exp_re, HC4_exp_im = PEISToNyquist(r"C:\Users\toggy\Desktop\
        OneDrive\Masteroppgave\NCA_Li-In_HC\HC_4_exp_fit_data\
        HC_4_exp.txt")
242 HC4_fit_re, HC4_fit_im = PEISToNyquist(r"C:\Users\toggy\Desktop\
        OneDrive\Masteroppgave\NCA_Li-In_HC\HC_4_exp_fit_data\
        HC_4_fit.txt")
243
244 HC6_15wt_re_19, HC6_15wt_im_19 = PEISToNyquist(r"C:\Users\toggy\
        Desktop\OneDrive\Masteroppgave\NCA_Li-In_HC\6_mg_load_HC_6\
        EIS_exp_data\19.txt")
245 HC6_15wt_fit_re_19, HC6_15wt_fit_im_19 = PEISToNyquist(r"C:\Users
        \toggy\Desktop\OneDrive\Masteroppgave\NCA_Li-In_HC\6
        _mg_load_HC_6\EIS_fits\Zfit_plots\HC6_19.txt")
246
247 HC8_3wt_re_19, HC8_3wt_im_19 = PEISToNyquist(r"C:\Users\toggy\
        Desktop\OneDrive\Masteroppgave\NCA_Li-In_HC\6_mg_load_HC_8\
        EIS_exp_data\19.txt")
248 HC8_3wt_fit_re_19, HC8_3wt_fit_im_19 = PEISToNyquist(r"C:\Users\
        toggy\Desktop\OneDrive\Masteroppgave\NCA_Li-In_HC\6
        _mg_load_HC_8\EIS_fits\Zfit_plots\HC8_19.txt")
249
250 textstr = '\n'.join((
251     '20th cycle, coated cells',
252     '26th cycle, uncoated cell'))
```

```python
253
254 fig , ax1 = plt.subplots(figsize = (6 ,6)) #9th cycle
255 ax1.scatter(HC4_exp_re/1000, HC4_exp_im/1000, marker='o', s = 20,
        facecolors = 'none', edgecolors = 'navy', label = 'NCA')
256 ax1.plot(HC4_fit_re/1000, HC4_fit_im/1000, color = 'dimgray',
        zorder = -1, label = 'Fit')
257 ax1.scatter(HC6_15wt_re_19[:55], HC6_15wt_im_19[:55], marker='o',
        s = 20, facecolors = 'none', edgecolors = 'royalblue', label
        = 'NCA 1.5')
258 ax1.plot(HC6_15wt_fit_re_19, HC6_15wt_fit_im_19, color = 'dimgray
        ', zorder = -1)
259 ax1.scatter(HC8_3wt_re_19[:55], HC8_3wt_im_19[:55], marker='o', s
        = 20, facecolors = 'none', edgecolors = 'lightskyblue',
        label = 'NCA 3')
260 ax1.plot(HC8_3wt_fit_re_19, HC8_3wt_fit_im_19, color = 'dimgray',
        zorder = -1)
261 ax1.set_xlabel('Z\' / k\u2126')
262 ax1.set_ylabel('-Z\'\' / k\u2126')
263 ax1.legend(loc = 'upper left', fontsize = 13, ncol = 1, frameon =
        False)
264 ax1.set_ylim(0, 17)
265 ax1.set_xlim(0, 17)
266 ax1.set_yticks([0.0, 2.5, 5.0, 7.5, 10.0, 12.5, 15.0])
267 ax1.text(0.6, 0.1, textstr, transform=ax1.transAxes, fontsize=13,
        verticalalignment='top')
268 left, bottom, width, height = [0.52, 0.5, 0.35, 0.35]
269 ax2 = fig.add_axes([left, bottom, width, height])
270 ax2.set_xlim(0, 320)
271 ax2.set_ylim(0, 320)
272 ax2.set_xticks([0, 100, 200, 300])
273 ax2.set_yticks([0, 100, 200, 300])
274 ax2.set_xlabel('Z\' / \u2126')
275 ax2.set_ylabel('-Z\'\' / \u2126')
276 ax2.scatter(HC4_exp_re, HC4_exp_im, marker='o', s = 20,
        facecolors = 'none', edgecolors = 'navy', label = 'NCA')
277 ax2.plot(HC4_fit_re, HC4_fit_im, color = 'dimgray', zorder = -1,
        label = 'Fit')
278 ax2.scatter(HC6_15wt_re_19[:55], HC6_15wt_im_19[:55], marker='o',
        s = 20, facecolors = 'none', edgecolors = 'royalblue', label
        = 'NCA 1.5')
279 ax2.plot(HC6_15wt_fit_re_19, HC6_15wt_fit_im_19, color = 'dimgray
        ', zorder = -1)
280 ax2.scatter(HC8_3wt_re_19[:55], HC8_3wt_im_19[:55], marker='o', s
        = 20, facecolors = 'none', edgecolors = 'lightskyblue',
```

```
      label = 'NCA 3')
281 ax2.plot(HC8_3wt_fit_re_19, HC8_3wt_fit_im_19, color = 'dimgray',
       zorder = -1)
282 plt.show()
283
284 'Coin cells longterm cycling of averages'
285 NCA_2102_2C_cyc, NCA_2102_2C_cap = GCPLToCycleCapacity(r"C:\Users
       \toggy\Desktop\OneDrive\Masteroppgave\Cycle data\Torgeir\2102
       _NCA_TMS\Cap_v_Cycle\2C_cycle1-100.txt")
286 NCA_2102_8C_cyc, NCA_2102_8C_cap = GCPLToCycleCapacity(r"C:\Users
       \toggy\Desktop\OneDrive\Masteroppgave\Cycle data\Torgeir\2102
       _NCA_TMS\Cap_v_Cycle\8C_cycle1-100.txt")
287 NCA_2102_10C_cyc, NCA_2102_10C_cap = GCPLToCycleCapacity(r"C:\
       Users\toggy\Desktop\OneDrive\Masteroppgave\Cycle data\Torgeir
       \2102_NCA_TMS\Cap_v_Cycle\10C_cycle1-100.txt")
288 NCA_2102_2C_eff = GCPLToEfficiency(r"C:\Users\toggy\Desktop\
       OneDrive\Masteroppgave\Cycle data\Torgeir\2102_NCA_TMS\
       Efficiency_v_Cycle\2C_cycle1-100.txt")
289 NCA_2102_8C_eff = GCPLToEfficiency(r"C:\Users\toggy\Desktop\
       OneDrive\Masteroppgave\Cycle data\Torgeir\2102_NCA_TMS\
       Efficiency_v_Cycle\8C_cycle1-100.txt")
290 NCA_2102_10C_eff = GCPLToEfficiency(r"C:\Users\toggy\Desktop\
       OneDrive\Masteroppgave\Cycle data\Torgeir\2102_NCA_TMS\
       Efficiency_v_Cycle\10C_cycle1-100.txt")
291 NCA_2102_avg_cap, NCA2102_dev_cap = AvgAndStdDevOfCapacities(
       NCA_2102_2C_cap, NCA_2102_8C_cap, NCA_2102_10C_cap)
292 NCA_2102_avg_eff, NCA2102_dev_eff = AvgAndStdDevOfCapacities(
       NCA_2102_2C_eff, NCA_2102_8C_eff, NCA_2102_10C_eff)
293
294 NCA_15wt_cs_1_cyc, NCA_15wt_cs_1_cap = GCPLToCycleCapacity(r"C:\
       Users\toggy\Desktop\OneDrive\Masteroppgave\2505_1.5wt_LYC\
       cyc_vs_cap\1.5wt_01.txt")
295 NCA_15wt_cs_1_eff = GCPLToEfficiency(r"C:\Users\toggy\Desktop\
       OneDrive\Masteroppgave\2505_1.5wt_LYC\cyc_v_eff\1.5wt_01.txt"
       )
296 NCA_15wt_cs_2_cyc, NCA_15wt_cs_2_cap = GCPLToCycleCapacity(r"C:\
       Users\toggy\Desktop\OneDrive\Masteroppgave\2505_1.5wt_LYC\
       cyc_vs_cap\1.5wt_02.txt")
297 NCA_15wt_cs_2_eff = GCPLToEfficiency(r"C:\Users\toggy\Desktop\
       OneDrive\Masteroppgave\2505_1.5wt_LYC\cyc_v_eff\1.5wt_02.txt"
       )
298 NCA_15wt_cs_3_cyc, NCA_15wt_cs_3_cap = GCPLToCycleCapacity(r"C:\
       Users\toggy\Desktop\OneDrive\Masteroppgave\2505_1.5wt_LYC\
       cyc_vs_cap\1.5wt_03.txt")
```

```
299  NCA_15wt_cs_3_eff = GCPLToEfficiency(r"C:\Users\toggy\Desktop\
         OneDrive\Masteroppgave\2505_1.5wt_LYC\cyc_v_eff\1.5wt_03.txt"
         )
300  NCA_15wt_cs_avg_cap, NCA_15wt_cs_dev_cap =
         AvgAndStdDevOfCapacities(NCA_15wt_cs_1_cap, NCA_15wt_cs_2_cap
         , NCA_15wt_cs_3_cap)
301  NCA_15wt_cs_avg_eff, NCA_15wt_cs_dev_eff =
         AvgAndStdDevOfCapacities(NCA_15wt_cs_1_eff, NCA_15wt_cs_2_eff
         , NCA_15wt_cs_3_eff)
302
303  NCA_3wt_cs_1_cyc, NCA_3wt_cs_1_cap = GCPLToCycleCapacity(r"C:\
         Users\toggy\Desktop\OneDrive\Masteroppgave\2505_3wt_LYC\
         cyc_v_cap\3wt_01.txt")
304  NCA_3wt_cs_2_cyc, NCA_3wt_cs_2_cap = GCPLToCycleCapacity(r"C:\
         Users\toggy\Desktop\OneDrive\Masteroppgave\2505_3wt_LYC\
         cyc_v_cap\3wt_02.txt")
305  NCA_3wt_cs_3_cyc, NCA_3wt_cs_3_cap = GCPLToCycleCapacity(r"C:\
         Users\toggy\Desktop\OneDrive\Masteroppgave\2505_3wt_LYC\
         cyc_v_cap\3wt_03.txt")
306  NCA_3wt_cs_avg_cap, NCA_3wt_cs_dev_cap = AvgAndStdDevOfCapacities
         (NCA_3wt_cs_1_cap, NCA_3wt_cs_2_cap, NCA_3wt_cs_3_cap)
307  NCA_3wt_cs_1_eff = GCPLToEfficiency(r"C:\Users\toggy\Desktop\
         OneDrive\Masteroppgave\2505_3wt_LYC\cyc_v_eff\3wt_01.txt")
308  NCA_3wt_cs_2_eff = GCPLToEfficiency(r"C:\Users\toggy\Desktop\
         OneDrive\Masteroppgave\2505_3wt_LYC\cyc_v_eff\3wt_02.txt")
309  NCA_3wt_cs_3_eff = GCPLToEfficiency(r"C:\Users\toggy\Desktop\
         OneDrive\Masteroppgave\2505_3wt_LYC\cyc_v_eff\3wt_03.txt")
310  NCA_3wt_cs_avg_eff, NCA_3wt_cs_dev_eff = AvgAndStdDevOfCapacities
         (NCA_3wt_cs_1_eff, NCA_3wt_cs_2_eff, NCA_3wt_cs_3_eff)
311  print(NCA_2102_avg_eff[0])
312  print(NCA_15wt_cs_avg_eff[0])
313  print(NCA_3wt_cs_avg_eff[1])
314
315  fig, ax1 = plt.subplots(figsize = (6,6))
316  ax1.errorbar(NCA_2102_2C_cyc[:len(NCA2102_dev_cap)],
         NCA_2102_avg_cap, yerr = NCA2102_dev_cap, ecolor = 'navy',
         color = 'navy', capsize = 2, marker = 'o', ms = 5, label = '
         2102 NCA')
317  ax1.errorbar(NCA_15wt_cs_1_cyc[:len(NCA_15wt_cs_dev_cap)],
         NCA_15wt_cs_avg_cap, yerr = NCA_15wt_cs_dev_cap, ecolor = '
         royalblue', color = 'royalblue', capsize = 2, marker = 'v',
         ms = 5, label = '2505 NCA 1.5')
318  ax1.errorbar(NCA_3wt_cs_1_cyc[:len(NCA_3wt_cs_dev_cap)],
         NCA_3wt_cs_avg_cap, yerr = NCA_3wt_cs_dev_cap, ecolor = '
```

June 26, 2022

```
      lightskyblue', color = 'lightskyblue', capsize = 2, marker =
      's', ms = 5, label = '2505 NCA 3')
319 ax1.set_ylabel('Discharge capacity / mAh g\u207B\u00B9')
320 ax1.set_xlabel('Cycle number')
321 # ax1.set_ylabel('Coulombic efficiency/%')
322 ax1.minorticks_on()
323 ax1.xaxis.set_tick_params(which='minor', bottom=False)
324 ax1.legend(loc = 'upper right', ncol = 1, fontsize = 13, frameon
      = False)
325 plt.show()
326
327 fig, ax1 = plt.subplots(figsize = (6,6))
328 ax1.errorbar(NCA_2102_2C_cyc[:len(NCA2102_dev_eff)],
      NCA_2102_avg_eff, yerr = NCA2102_dev_eff, ecolor = 'navy',
      color = 'navy', capsize = 2, marker = 'o', ms = 5, label = '
      2102 NCA')
329 ax1.errorbar(NCA_15wt_cs_1_cyc[:len(NCA_15wt_cs_dev_eff)],
      NCA_15wt_cs_avg_eff, yerr = NCA_15wt_cs_dev_eff, ecolor = '
      royalblue', color = 'royalblue', capsize = 2, marker = 'v',
      ms = 5, label = '2505 NCA 1.5')
330 ax1.errorbar(NCA_3wt_cs_1_cyc[:len(NCA_3wt_cs_dev_eff)],
      NCA_3wt_cs_avg_eff, yerr = NCA_3wt_cs_dev_eff, ecolor = '
      lightskyblue', color = 'lightskyblue', capsize = 2, marker =
      's', ms = 5, label = '2505 NCA 3')
331 ax1.set_xlabel('Cycle number')
332 ax1.set_ylabel('Coulombic efficiency / %')
333 ax1.minorticks_on()
334 ax1.xaxis.set_tick_params(which='minor', bottom=False)
335 ax1.legend(loc = 'upper left', ncol = 3, fontsize = 11, frameon =
       False)
336 plt.show()
337
338 'EIS coin cell exp and fit'
339 exp_10C_real, exp_10C_im = PEISToNyquist(r"C:\Users\toggy\Desktop
      \OneDrive\Masteroppgave\Cycle data\Torgeir\2102_NCA_TMS\PEIS
      \2102_NCA_10C_uncycled.txt")
340 exp_10C_cycled_real, exp_10C_cycled_im = PEISToNyquist(r"C:\Users
      \toggy\Desktop\OneDrive\Masteroppgave\Cycle data\Torgeir\2102
      _NCA_TMS\PEIS\2102_NCA_10C_cycled.txt")
341 fit_10C_real, fit_10C_im = PEISToNyquist(r"C:\Users\toggy\Desktop
      \OneDrive\Masteroppgave\Cycle data\Torgeir\2102_NCA_TMS\PEIS
      \2102_NCA_10C_uncycled_fit.txt")
342 fit_10C_cycled_real, fit_10C_cycled_im = PEISToNyquist(r"C:\Users
      \toggy\Desktop\OneDrive\Masteroppgave\Cycle data\Torgeir\2102
```

```python
      _NCA_TMS\PEIS\2102_NCA_10C_cycled_fit.txt")

exp_15wt_real , exp_15wt_im = PEISToNyquist(r"C:\Users\toggy\
    Desktop\OneDrive\Masteroppgave\2505_1.5wt_LYC\EIS\1.5
    wt_01_before.txt")
exp_15wt_cycled_real , exp_15wt_cycled_im = PEISToNyquist(r"C:\
    Users\toggy\Desktop\OneDrive\Masteroppgave\2505_1.5wt_LYC\EIS
    \1.5wt_01_after.txt")
fit_15wt_real , fit_15wt_im = PEISToNyquist(r"C:\Users\toggy\
    Desktop\OneDrive\Masteroppgave\2505_1.5wt_LYC\EIS\1.5
    wt_01_before_fit.txt")
fit_15wt_cycled_real , fit_15wt_cycled_im = PEISToNyquist(r"C:\
    Users\toggy\Desktop\OneDrive\Masteroppgave\2505_1.5wt_LYC\EIS
    \1.5wt_01_after_fit.txt")

exp_3wt_real , exp_3wt_im = PEISToNyquist(r"C:\Users\toggy\Desktop
    \OneDrive\Masteroppgave\2505_3wt_LYC\EIS\3wt_03_before.txt")
exp_3wt_cycled_real , exp_3wt_cycled_im = PEISToNyquist(r"C:\Users
    \toggy\Desktop\OneDrive\Masteroppgave\2505_3wt_LYC\EIS\3
    wt_03_after.txt")
fit_3wt_real , fit_3wt_im = PEISToNyquist(r"C:\Users\toggy\Desktop
    \OneDrive\Masteroppgave\2505_3wt_LYC\EIS\3wt_03_before_fit.
    txt")
fit_3wt_cycled_real , fit_3wt_cycled_im = PEISToNyquist(r"C:\Users
    \toggy\Desktop\OneDrive\Masteroppgave\2505_3wt_LYC\EIS\3
    wt_03_after_fit.txt")

fig , ax1 = plt.subplots(figsize = (6,6))
# left , bottom , width , height = [0.35, 0.35, 0.4, 0.4]
# ax2 = fig.add_axes([left, bottom, width, height])
# ax1.scatter(exp_10C_real[:len(fit_10C_real)], exp_10C_im[:len(
    fit_10C_real)], marker='o', s = 25, facecolors = 'none',
    edgecolors = 'navy', label = '2102 NCA Exp')
# ax1.scatter(exp_15wt_real[:len(fit_15wt_real)], exp_15wt_im[:
    len(fit_15wt_real)], marker='o', s = 25, facecolors = 'none',
     edgecolors = 'royalblue', label = '2505 NCA 1.5 Exp')
# ax1.plot(fit_15wt_real, fit_15wt_im, color = 'dimgray', zorder
    = -3)
# ax1.scatter(exp_3wt_real[:len(fit_3wt_real)], exp_3wt_im[:len(
    fit_3wt_real)], marker='o', s = 25, facecolors = 'none',
    edgecolors = 'lightskyblue', label = '2505 NCA 3 Exp')
# ax1.plot(fit_3wt_real, fit_3wt_im, color = 'dimgray', zorder =
    -2)
```

85

```
362  # ax1.plot(fit_10C_real, fit_10C_im, color = 'dimgray', label = '
         Fit', zorder = -1)
363  ax1.scatter(exp_10C_cycled_real[:len(fit_10C_cycled_real)],
         exp_10C_cycled_im[:len(fit_10C_cycled_real)], marker='o', s =
          25, facecolors = 'none', edgecolors = 'navy', label = '2102
         NCA')
364  ax1.plot(fit_10C_cycled_real, fit_10C_cycled_im, color = 'dimgray
         ', label = 'Fit', zorder = -1)
365  ax1.scatter(exp_15wt_cycled_real[1:len(fit_15wt_cycled_real)],
         exp_15wt_cycled_im[1:len(fit_15wt_cycled_real)], marker='o',
         s = 25, facecolors = 'none', edgecolors = 'royalblue', label
         = '2505 NCA 1.5')
366  ax1.plot(fit_15wt_cycled_real, fit_15wt_cycled_im, color = '
         dimgray', zorder = -3)
367  ax1.scatter(exp_3wt_cycled_real[1:len(fit_3wt_cycled_real)],
         exp_3wt_cycled_im[1:len(fit_3wt_cycled_real)], marker='o', s
         = 25, facecolors = 'none', edgecolors = 'lightskyblue', label
          = '2505 NCA 3')
368  ax1.plot(fit_3wt_cycled_real, fit_3wt_cycled_im, color = 'dimgray
         ', zorder = -2)
369  ax1.set_xlabel('Z\' / \u2126')
370  ax1.set_ylabel('-Z\'\' / \u2126')
371  ax1.legend(loc = 'upper left', fontsize = 13, ncol = 1, frameon =
          False)
372  ax1.set_ylim(0, 185)
373  ax1.set_xlim(0, 185)
374  ax1.set_xticks([0, 25, 50, 75, 100, 125, 150, 175])
375  plt.show()
376
377  'LYC LPSC 250 MPa EIS'
378  LYC_df = pd.read_excel(r"C:\Users\toggy\Desktop\OneDrive\
         Masteroppgave\EIS 035\LYC_w_YCl3_2000kg_EIS.xlsx", skiprows
         =3)
379  LYC_data = LYC_df.to_numpy()
380  LPSC_df = pd.read_csv(r"C:\Users\toggy\Desktop\OneDrive\
         Masteroppgave\Torgeir_Biologic_003\EIS LPSC under pressure\
         LPSC_FREQ_REAL.txt", sep = '\t', skiprows=1)
381  LPSC_data = LPSC_df.to_numpy()
382  LPSC_factor = 0.039/(np.pi*0.5**2)
383  LYC_factor = 0.079/(np.pi*0.5**2)
384  'Bode LPSC'
385  fig, ax1 = plt.subplots(figsize = (6,6))
386  ax1.scatter(np.log10(LPSC_data[:,0]), LPSC_factor/LPSC_data[:,1],
          marker = 's', s = 15, c = 'royalblue', label = 'LPSC')
```

```python
387 ax1.scatter(np.log10(LYC_data[:,1]), LYC_factor/LYC_data[:,2],
        marker = 'o', s = 15, c = 'lightskyblue', label = 'LYC')
388 ax1.set_yscale('log')
389 ax1.axhline(y = 0.00171, color = 'royalblue', linestyle = 'dashed
        ', xmax = 0.7)
390 ax1.axhline(y = 0.000125, color = 'lightskyblue', linestyle = '
        dashed', xmax = 0.7)
391 ax1.set_xlim(2, 6)
392 ax1.set_ylim(5*10**(-5), 5*10**(-3))
393 ax1.set_xlabel('log( \u03BD / Hz )')
394 ax1.set_ylabel('\u03C3\' / S cm\u207B\u00B9')
395 ax1.legend(loc = 'upper right', ncol = 1, fontsize = 13, frameon
        = False)
396 plt.show()
```